The Effect of Soil Moisture and Vegetation Heterogeneity on a Great Plains Dryline: a Numerical Study

by
Brent L. Shaw

Department of Atmospheric Science
Colorado State University
Fort Collins, Colorado

Roger A. Pielke, P.I.
National Science Foundation Grant No. ATM-9306754

Colorado State University

Department of Atmospheric Science

Paper No. 576

THE EFFECT OF SOIL MOISTURE AND VEGETATION HETEROGENEITY ON A GREAT PLAINS DRYLINE: A NUMERICAL STUDY

Brent L. Shaw

Department of Atmospheric Science
Colorado State University
Fort Collins, Colorado
Summer 1995

Atmospheric Science Paper No. 576

ABSTRACT

THE EFFECT OF SOIL MOISTURE AND VEGETATION HETEROGENEITY ON A GREAT PLAINS DRYLINE: A NUMERICAL STUDY

The impact of heterogeneous soil moisture and vegetation fields on a Great Plains dryline are examined through the use of a mesoscale numerical model.

A three dimensional, non-hydrostatic, nested grid version of the Colorado State University Regional Atmospheric Modeling System (RAMS) was used to perform five simulations of an actual dryline which was observed as part of the COPS-91 field experiment on 15 May 1991. A control run which was designed to reproduce the observed conditions as accurately as possible was generated and verified against standard National Weather Service observations, PAM-II observations, M-CLASS soundings, and vertical cross section analyses obtained from the NOAA P-3 aircraft. A representative heterogeneous soil moisture field for use in the control simulation was generated using an antecedent precipitation index (API). Variable vegetation was input using the Biosphere-Atmosphere Transfer Scheme (BATS) and included 18 categories of land surface type derived from the USGS NDVI dataset. Because the standard RAMS code modifies the surface fluxes by the Leaf Area Index (LAI), the LAI was limited to a value of 3.0 or less in the flux calculations for all vegetation types although the BATS scheme assigns values of LAI as high as 6.0. Justification for this limitation is presented.

Four additional simulations were performed as sensitivity tests and compared to the control simulation. Two of the simulations involved perturbations of the initial

soil moisture field. One was performed using the same heterogeneous field as the control run but was reduced at all grid points by a factor of 0.5. The second utilized a homogeneous initialization of soil moisture using a very low (i.e., dry) value. The remaining two simulations focused on the variable vegetation impact. One utilized a homogeneous vegetation type of short grass and the other used variable vegetation, but without the imposed limit on LAI in the surface flux calculations used in the control run. Comparisons of the standard meteorological variables are made, including various stability parameters, kinematic variables, and the surface sensible and latent heat fluxes.

Results of this research indicate that the use of realistic heterogeneous soil moisture and vegetation may be extremely important for accurate prediction of dryline formation and morphology. The effect of variable soil moisture appears to be first order, with large impacts on the strength of the thermal and moisture gradients along the dryline and the actual position of the dryline. The effect of variable vegetation appears to be second order, with the main impact being on the heterogeneity of the surface fluxes and wind field. This could presumably impact how well the model forecasts the exact location of areas favorable for convection. The results also justify the need for better parameterizations of the vegetation canopy influences on the atmosphere, as well as the need for better methods of generating representative soil moisture fields.

Brent L. Shaw
Department of Atmospheric Science
Colorado State University
Fort Collins, Colorado 80523
Summer 1995

ACKNOWLEDGEMENTS

I wish to first gratefully thank my adviser, Professor Roger A. Pielke, for the guidance provided to me during the course of my research. It was his idea that I pursue the dryline study, and I am pleased his direction. Special thanks are due to Dr. Conrad Ziegler of the National Severe Storms Laboratory. Not only did he host me during VORTEX-94 and serve as a committee member, he worked with me in the unofficial role of co-adviser. His guidance and thought provoking questions of me were never more than a keystroke away via the "information superhighway". I also appreciate the comments and critiques of my other committee members, Professors Richard Johnson and William Lauenroth. It is only under the guidance of a scrutinous committee that quality research is performed. Although not a committee member, Professor William Parton's advice concerning the interpretation of the Beer-Bougher Law and the effect of Leaf Area Index on the surface fluxes is also appreciated.

There are many other people that need to be thanked. I am sure I will inadvertently leave some of you out, so please accept my apologies if I do. Thanks go to Dr. Jeff Copeland for showing me how to use the RAMS model and for always taking the time to answer my plethora of questions. Louis Grasso deserves many thanks for helping me get the model configured and running for this particular case study. Dr. John Lee provided the code and guidance for generating the API analyses used in the simulations. Tom Chase and Cathy Finley were always ready and willing to share their knowledge of the often cryptic code when I was stuck on a problem, and their help is deeply appreciated. Dr. Bob Walko also deserves thanks for his

patience. It seems as if he always walked around the corner just when I needed some guidance concerning the operation of RAMS, bug fixes, etc. Donna Chester deserves a huge box of chocolate for her patience in dealing with my inadequate knowledge of UNIX and how to perform simple data backup operations. I would also like to thank Dallas McDonald for all of her work in typesetting the final copy of this thesis. Without her diligent work, the finished product would probably not be finished for another year.

My stay at Colorado State University was funded by the Air Force Institute of Technology. It is my hope that the results of my research can directly benefit Air Force and Department of Defense operations. Additional support was received from National Science Foundation Grant #ATM-930675 and United States Geological Survey (USGS) Grant #1434-94-A-1275. The observational data used for model initialization and verification were obtained from the National Center for Atmospheric Research (NCAR). NCAR is partially supported by the National Science Foundation. Vegetation, land-percentage, and topographic data were obtained from the USGS.

Finally, I would like to thank my wife, Ashley, for all of her support and understanding. I don't know how I will ever repay her for her cheerfulness and encouragement during the stress of my classes and the final push to finish my thesis. How she managed to maintain a great attitude while suffering from sleep deprivation associated with being a new mother, I will never know. It is only through her encouragement that this research was completed successfully.

TABLE OF CONTENTS

LIST OF TABLES

LIST OF FIGURES

Chapter 1

INTRODUCTION

1.1 Purpose of Research

The term "dryline", apparently first coined by McGuire (1962), refers to a narrow zone containing a sharp gradient of moisture in the planetary boundary layer. In this paper, the term will generically refer to the drylines which occur in the Great Plains of the United States, although similar features are observed worldwide (Schaefer 1986). The dryline has been called by various names, including dewpoint front (Beebe 1958), dry front (Fujita 1958), and even Marfa front (Matteson 1968) because the town of Marfa, Texas is often affected by drylines. The dryline boundary separates the drier air originating over the Mexican Plateau and the U.S. intermountain region from the moist air that originates over the Gulf of Mexico (Schaefer 1986). The sharpness of the dewpoint gradient has been documented by several observational studies (e.g., NSSP Staff 1963; Parsons et al. 1991; Ziegler and Hane 1993; Hane et al. 1993) to be up to several $^{\circ}$ C km^{-1}, much larger than the May climatological average of 0.04°C km^{-1} for this region (Dodd 1965).

Because drylines play a significant role in the generation of thunderstorms in the Great Plains of the United States (Rhea 1966; Bluestein and Parker 1993), they have long been an object of observational and numerical studies. The recent advances in computing power have allowed the use of mesoscale numerical models to explicitly resolve features of the dryline which cannot be directly observed due to coarse horizontal spacing of observation platforms. Many of these features have been verified through the use of mobile sounding laboratories, aircraft observations,

Doppler lidar, and observations collected by meso-networks. As numerical studies continue to gain credibility from the results of intensive observational studies, they can be used to provide insight as to the structure and evolution of a typical dryline. Results from such studies should enhance our understanding and ability to predict dryline location, evolution, and associated weather more accurately using numerical methods and facilitate design of future mesoscale field studies.

The research presented here consists of several numerical simulations of a dryline which occurred over the Southern Great Plains of the United States on 15 May 1991. These simulations were performed using a three-dimensional, primitive equation, mesoscale model. A control simulation was generated with the goal of reproducing the observed conditions as accurately as possible. The remaining simulations were completed using variations from the control simulation of soil moisture and vegetation type in the model initialization. The purpose of the simulations is to determine what, if any, significant impact the use of realistic heterogeneous soil moisture and vegetation fields in the model may have on a simulated dryline. The results may then be used to speculate on how the formation and evolution of actual drylines are effected by soil moisture and vegetation.

This research project has several goals. First, the control simulation will be used to identify strengths and weaknesses of how this particular model handles the inclusion of heterogeneous land-surface variables by evaluating parameters related to the observed and modeled surface energy budget. Second, the sensitivity tests will illustrate the importance of including land-surface parameterizations in mesoscale simulations of drylines. Third, the simulations will provide greater understanding of the structure and evolution of the dryline. Hopefully, the results of this research will eventually lead to improvements in our ability to both understand and forecast drylines and other boundary layer phenomena which may be sensitive to heterogeneous land-surface conditions.

The following two sections of this chapter discuss some of the previous research pertaining to drylines and land-surface influences on mesoscale weather. Chapter Two describes the control (CONT) simulation, including the meteorological conditions for the case study, the model used, and the verification and results of the simulation. Chapter Three describes the sensitivity tests performed while Chapter Four presents the detailed results and comparisons to the CONT simulation. The final chapter summarizes the results and conclusions and presents suggestions for future work.

1.2 Drylines

Drylines differ from synoptic thermal fronts in that the temperature gradient exhibits a diurnal variation in sign. During the daylight hours, the drier air to the west is able to heat more rapidly than the moist air to the east, resulting in warmer air to the west of the dryline. After sunset, the dry air to the west is also able to cool more rapidly, so that by morning the temperature gradient is reversed. There is also a diurnal variation in the movement of drylines. Drylines tend to move east during the morning and afternoon hours, becoming stationary during the late afternoon. During the night drylines retrogress back to the west. This process repeats each day until a synoptic frontal system passes through the region from the north, thus displacing the contrasting airmasses defining the dryline.

Because of the dependence of moist air density upon both temperature and water vapor content, there is not a significant difference in density across the afternoon dryline (Schaefer 1975). This is different from classical fronts. The lack of a density gradient results in the virtual isentropes being nearly vertical throughout the lowest 1-2 km at the dryline. This vertical structure has been supported by many studies (e.g., Ogura and Chen 1977, McCarthy and Koch 1982; Ziegler and Hane 1993) and is in contrast with the original model proposed by Carlson and Ludlam (1968). Additionally, Ogura and Chen (1977) found that there is a maximum in

virtual potential temperature in the boundary layer just west of the dryline. This feature is consistent with Carlson and Ludlam (1968). Apparently, there may be various types of drylines which need to be classified.

The eastward motion of the dryline under synoptically quiescent conditions is hypothesized to be the result of vertical mixing, first proposed by Schaefer (1974a). In the morning, the western edge of the moist air is very shallow, due to the higher terrain of the region immediately east of the Rocky Mountains. This shallow layer of moist air is quickly eroded by vertical mixing of the dry air aloft, resulting in a rapid eastward progression of the dryline. Because the terrain elevation continues to decrease as the dryline moves east, the moist layer becomes deeper, and vertical mixing becomes less efficient. Eventually, for reasons not fully understood, the dryline becomes stationary and continues to maintain a strong moisture gradient, even in the presence of continued vertical mixing. At this mature stage, strong contrasts in moisture, temperature, and wind exist in the general vicinity of the dryline.

The narrow zone along and just east of the dryline is characterized by strong convergence and large vertical motions. Many studies have shown vertical velocities ranging from 1 to 5 m s^{-1} (Ziegler and Hane 1993; Ziegler et al. 1995; Parsons et al. 1991). There is often a band of convective clouds associated with this zone along the dryline. The presence of these convective clouds, often even after thunderstorms have formed and moved east, suggests that there is a lifting mechanism intrinsic to the dryline itself (Schaefer 1986). The nature of this mechanism, however, is not clearly understood.

Schaefer (1975) hypothesized that a "nonlinear biconstituent diffusion mechanism" is responsible for producing positive buoyant updrafts along the dryline. However, Lilly and Gal-Chen (1990) discounted this mechanism, arguing that it would actually produce weak negative buoyancy. Another possible source is the

solenoidal mechanism (Sun and Ogura 1979; Sun and Wu 1992; Ziegler and Hane 1993; Ziegler et al. 1995). This mechanism requires that a persistent gradient in virtual potential temperature throughout the lower troposphere exist in the vicinity of the dryline with cooler air to the east.

Many studies have found virtual potential temperature gradients in conjunction with drylines (Ziegler and Hane 1993; Ogura and Chen 1977). Ogura and Chen (1977) argued that this gradient contributed to the rapid increase of convergence due to the "inland sea-breeze" effect (sea breezes are discussed in Estoque 1962; Pielke 1974). Numerical studies (e.g. Anthes et al. 1982; Benjamin 1986; Benjamin and Carlson 1986; Sun and Wu 1992; Ziegler et al. 1995) have also supported the notion that this solenoidal mechanism is responsible for generating convergence and hence increasing the moisture gradient and vertical motion along the dryline. On the other hand, while investigating this problem with high resolution, two-dimensional numerical simulations, the results of Ziegler et al. (1995) showed no apparent relationship between the peak updraft strength and the local solenoids of pressure and virtual potential temperature at the dryline. They argued that the gradient of mean boundary layer virtual temperature east of the dryline results in a mesoscale hydrostatic pressure gradient. This causes an upslope flow to develop, which terminates abruptly at the dryline, focusing convergence and vertical motion at this location. This process then leads to increased thermal contrasts across the dryline by kinematic frontogenetic forcing.

Regardless of the controversy, it is generally accepted that the land surface plays a significant role in the generation of drylines. A primary effect is through topography. As mentioned above, drylines in the U.S. occur only in the High Plains region, and rarely ever occur farther east than 95 degrees west longitude. It is in this region of the U.S. that the terrain slopes gently upward from east to west, allowing the vertical mixing mechanism for dryline motion mentioned above to oc-

cur. Schaefer (1986) describes dryline formation as a frontogenetic process due to inhomogeneities in the wind field which are directly related to the sloping terrain.

Numerical studies by Sun and Wu (1992) found additional essential ingredients for the formation of drylines. They concluded that the three most important factors in dryline formation and sustenance of the moisture gradient are the presence of low-level vertical wind shear, the sloping terrain, and a gradient in soil moisture. With these three features present, an initial gradient of atmospheric moisture was not a requirement for the generation of a dryline. These findings regarding the impact of shear, terrain, and soil moisture were confirmed by Ziegler et al. (1995),

In this study, we further investigate the role that variable soil moisture plays in the morphology of drylines. Additionally, since the transport of moisture from the soil to the atmosphere is largely due to vegetation through the transpiration process, we also investigate the effect of different vegetation fields on the evolution of the dryline.

1.3 Significance of Heterogeneous Soil Moisture and Vegetation

Pielke and Segal (1986) showed that mesoscale circulations due to differential heating of the terrain can be significant. The principal method for creating differential heating is through heterogeneous surface characteristics. There has been much effort in recent years to include land-surface information in numerical models, from microscale simulations through large scale climate simulations (e.g., Avissar and Pielke 1989; Li and Avissar 1994; Kosta and Suarez 1992; Bonan et al. 1993; Pleim and Xiu 1995, Pitman 1994). This work has focused on issues such as the effect of land use on regional climate (e.g., Avissar and Pielke 1989; Pielke and Avissar 1990; Anthes 1984; Yan and Anthes 1988, Garrett 1982) and the improvement of numerical simulations for prediction purposes (Lee 1992; Pielke et al. 1994; Smith et al. 1994). Other studies suggest that the soil moisture field may be the most

important parameter in determining the structure of the daytime boundary layer (e.g., McCumber and Pielke 1981; Zhang and Anthes 1982; Clark and Arritt 1995).

Chang and Wetzel (1991) argued that the proper representation of evapotranspiration processes from the soil through vegetation canopies into the atmosphere is essential to mesoscale models which try to predict prestorm environments. Using the Goddard mesoscale model (GMASS), they performed sensitivity test simulations of a prestorm environment that spawned a severe storm in Nebraska. Three simulations were performed; one with variable vegetation cover and soil moisture (VEG), one with variable soil moisture and no vegetation (NOVEG), and one with homogeneous vegetation and soil moisture (NOSPA). Although in all three of the simulations conditions favorable for severe storm initiation developed, the VEG and NOVEG runs produced small scale features in the divergence field which were not present in the NOSPA run. They concluded that even though the differential heating due to soil and vegetation variations are a secondary effect, these effects are likely to be critical in determining the location and time of the first development of potentially severe thunderstorms.

Lanicci et al. (1987) presented results of three-dimensional simulations they performed using the Pennsylvania State/NCAR regional model. In their work, they also performed sensitivity tests on the dryline by comparing a control run which utilized a climatologically derived soil moisture distribution to several runs with perturbed soil moisture fields. They found that variations in soil moisture have a large effect on the dryline environment. Specifically, they concluded:

> "The soil-moisture gradient over Texas and Oklahoma influences the processes of differential surface heating and vertical mixing, which are important in the daytime movement of the dryline. Low soil moisture over west Texas and northern Mexico causes an enhancement of easterly ageostrophic flow over east Texas and the Gulf of Mexico by allowing strong surface heating to occur over west Texas and northern Mexico. This easterly ageostrophic flow is shown to contribute to advecting the dryline westward during the early evening. The location and intensity of

> moist convection...is sensitive to soil moisture distributions over Mexico and Texas because the lid strength is influenced by both the low-level moisture over Texas and the potential temperature of the Mexican air."

They stated three major implications of their results. First, an accurate representation of the soil moisture is necessary for accurate prediction of the PBL and severe storm environment. Second, they concluded that anomalously dry or wet regional conditions can cause shifts in the low-level moisture convergence areas, thereby enhancing drought/flood conditions in other areas. Third, they suggested that convective rainfall patterns may be altered by regional-scale irrigation practices.

Ziegler et al. (1995) performed two-dimensional, high resolution simulations of a dryline and compared their results with special airborne and sounding observations. Their study addressed the impact of east-west soil moisture variability and vegetation on the evolution of the convective boundary layer and dryline formation. Their results suggested a strong sensitivity of the dryline to soil moisture. For classical dryline formation, a west to east gradient in volumetric soil moisture of 0.15 (50 km)$^{-1}$ was required. Without soil moisture gradients, they observed the formation of "non-classical" drylines, with strong convergence and updrafts co-located with weak moisture gradients. They also found a sensitivity to vegetation contrasts, due to the accentuation of the variation of sensible heat flux in the surface layer. Their conclusions support the findings of Lanicci et al. (1987).

The research presented in the current study will expand on the work of Ziegler et al. (1995) by incorporating a three-dimensional model and realistic soil moisture and vegetation distributions. It will also improve upon the work performed by Lannici et al. (1987) by utilizing a much finer grid, more spatially detailed vegetation distributions, and a more representative soil moisture distribution to resolve some of the fine-scale features.

Chapter 2

THE CONTROL SIMULATION

2.1 Observed Synoptic Meteorological Conditions on 15 May 1991

The particular dryline that serves as the focus of this study was intensely observed as part of the COPS-91 field experiment (Hane et al. 1993). In addition to standard hourly NWS surface observations, data were also collected by the PAM-II network (Brock et al. 1986), M-CLASS sounding units (Rust et al. 1990), and the NOAA P-3 research aircraft. Data collection schemes employed on this day are described in Hane et al. (1993).

All of the analyses of the observations shown in this section include data obtained from both the NWS standard network and the PAM-II network. Figure 2.1 shows the surface temperature and dewpoint analyses for 1200 UTC, 15 May 1991. This corresponds to the initialization time for all of the simulations. A cold front extended southwest across New Mexico from a low pressure center located in south-central Colorado. The dryline, which was rather diffuse at this time, can be seen as a dewpoint gradient occurring from eastern Colorado south along the Texas-New Mexico border. Dewpoints were relatively constant east of this zone, with values ranging from 16 to 19°C across the Texas Panhandle and western Oklahoma. West of the dryline, dewpoint temperatures ranged from -3 to -13°C across New Mexico and Colorado. Temperatures east of the cold front were also relatively constant, ranging from 15 to 20°C. Winds east of the dryline were generally southerly or southeasterly. Westerly winds were observed west of the dryline.

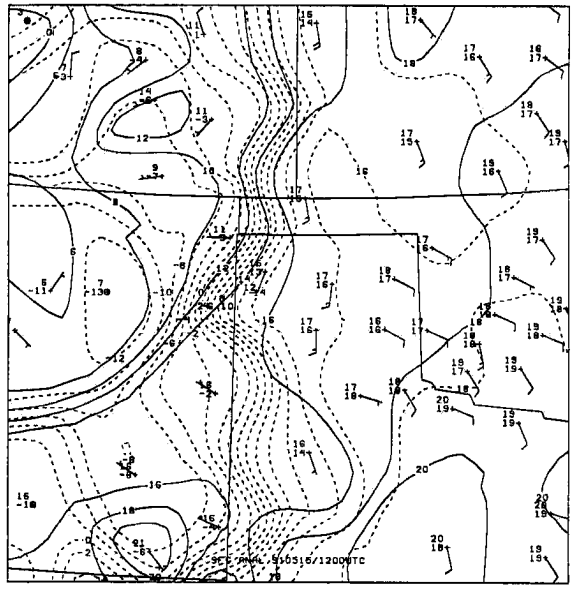

Figure 2.1: Station plots and objective analysis of temperature and dewpoint (°C) for 1200 UTC, 15 May 1991. Wind barbs are in knots. Contour interval is 2°C. Data obtained from NWS and PAM-II observations available through NCAR.

Figure 2.2 shows the temperature and dewpoint analyses for 1500 UTC through 0000 UTC. By 1500 UTC, the southern half of the dryline had already moved nearly 100 km east to the central Texas Panhandle. A zone of confluent winds along the moisture gradient had also become more pronounced, with southeasterly winds to the east and west-southwesterly winds to the west. A distinct tongue of warm air was analyzed just to the west of the confluent zone. Temperatures in the western Texas Panhandle had risen rapidly to around 24°C, while the temperatures in the eastern Texas Panhandle and western Oklahoma continued to hover around 20°C. Also note the pocket of slightly cooler air analyzed over the east-central Texas Panhandle and southwest Oklahoma.

By 1800 UTC, the entire dryline was becoming very distinct from southwest Kansas south through the central Texas Panhandle. The dewpoint temperatures varied by nearly 20°C across the Texas Panhandle. The thermal tongue continued to persist, providing the typical dryline scenario of warm temperatures to the west

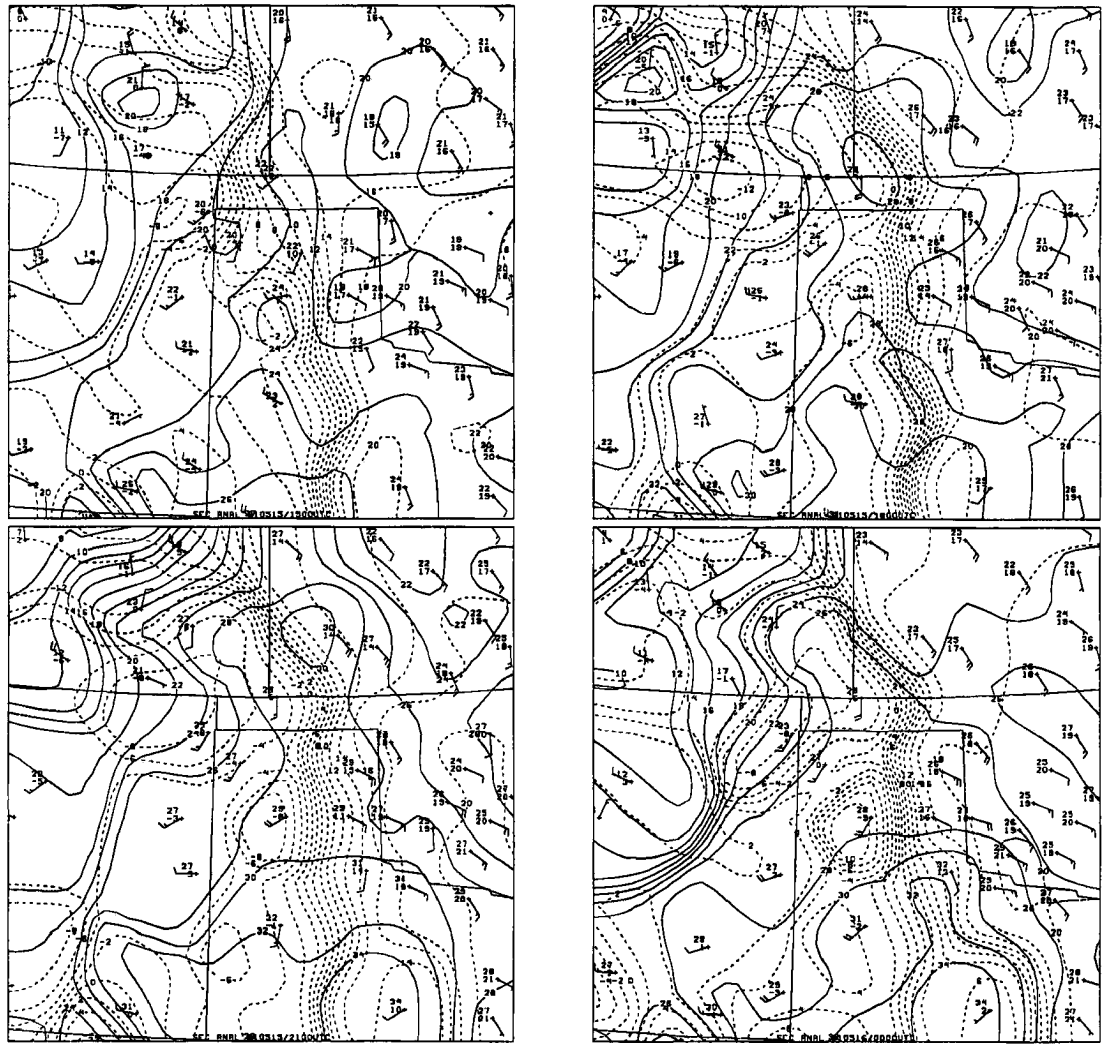

Figure 2.2: Same as 2.1 for 1500 UTC (top-left), 1800 UTC (top-right), 2100 UTC (bottom-left), and 0000 UTC (bottom-right). Data obtained from NWS and PAM-II observations available through NCAR.

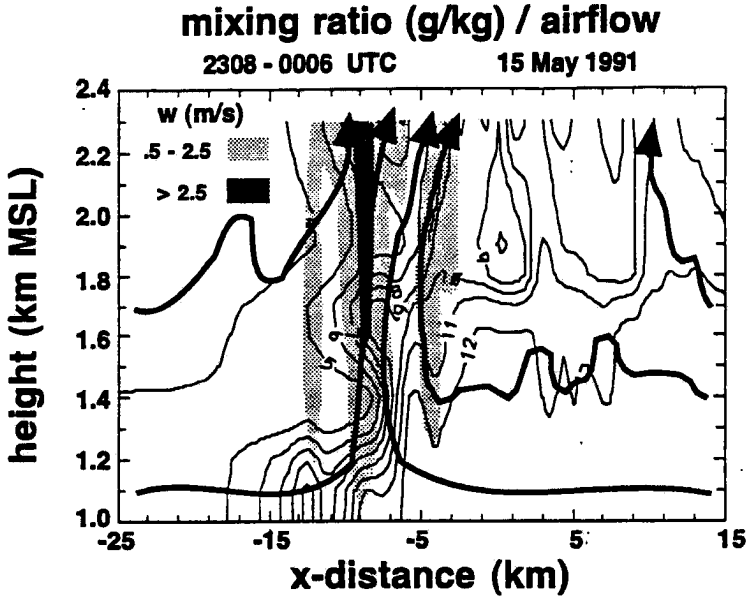

Figure 2.3: Vertical cross section analysis of water vapor mixing ratio (g kg^{-1}) from aircraft traverses of the dryline between 2308 UTC, 15 May, and 0006 UTC, 16 May. Selected streamlines are included and areas of upward motion shaded (after Hane et al. 1993).

and cooler temperatures to the east. Throughout the remainder of the afternoon, the location of the dryline remained nearly stationary as the moisture gradient continued to increase. It is important to point out that the objective analyses shown do not capture the actual fine scale structure of the moisture gradient due to coarse observation spacing and filtering with interpolation of data to the analysis grid. Aircraft and M-CLASS sounding information revealed that the moisture gradient along the dryline as shown in the analyses here actually occurred on a scale of less than 30 km, which is consistent with many of the dryline studies mentioned in the previous chapter and the model results of this study.

Figure 2.3 is a vertical cross section derived from data collected by the P-3 in the late afternoon (Hane et al. 1993). Because each traverse took about 1 hour to complete, and because the vertical resolution was relatively coarse (about 300 m) there is some error in this analysis due to evolution and movement. However, it does capture the general structure of the dryline during the late afternoon. The surface mixing ratio gradient was approximately 0.60 g kg^{-1} km^{-1}. Co-located with the

moisture gradient was a strong updraft, exceeding 2.5 m s^{-1} at 1 km AGL. Notice also the upward bulge of moisture in this same location.

The vertical structure of the environments east and west of the dryline can be seen in the two soundings shown in Figure 2.4. These soundings were obtained from the two M-CLASS stations around 2300 UTC. The soundings were located approximately 75 km apart, so the extreme gradient in moisture is also readily apparent, as the difference in dewpoint across this distance was 21°C. The sounding west of the dryline indicates that the atmosphere was well mixed throughout the depth of the troposphere. The temperature lapse rate was super-adiabatic near the surface and nearly dry-adiabatic throughout the remainder of the troposphere. Winds were southwesterly throughout the depth of the sounding, and the moisture profile suggests that subsidence may have been occurring. East of the dryline, a weak inversion was present from about 825 to 800 mb. Above the inversion, the profile is very similar to the profile west of the dryline, although it is more moist and has a slightly lower temperature lapse rate. This may be due to the advection of moisture eastward from the bulge of moisture aloft which occurred at the dryline (Ziegler and Hane 1993). Below the inversion, winds were southeasterly, with southwesterly winds above the inversion. Calculation of the convective available potential energy (CAPE) using the average temperature and moisture values in the lowest 1 km from these two soundings supports the findings of Ziegler et al. (1995) that this variable experiences significant gradients within a few tens of kilometers east of the dryline. CAPE increased from 0 J kg^{-1} at the western location to 1839 J kg^{-1} at the eastern location.

Since the region was unaffected by upper air disturbances on this particular day, convection was locally forced by convergence at the dryline. Moderate convection developed in the immediate vicinity of the dryline. Deep convective clouds began developing between 1930 UTC and 2000 UTC, with the deepest convection along the

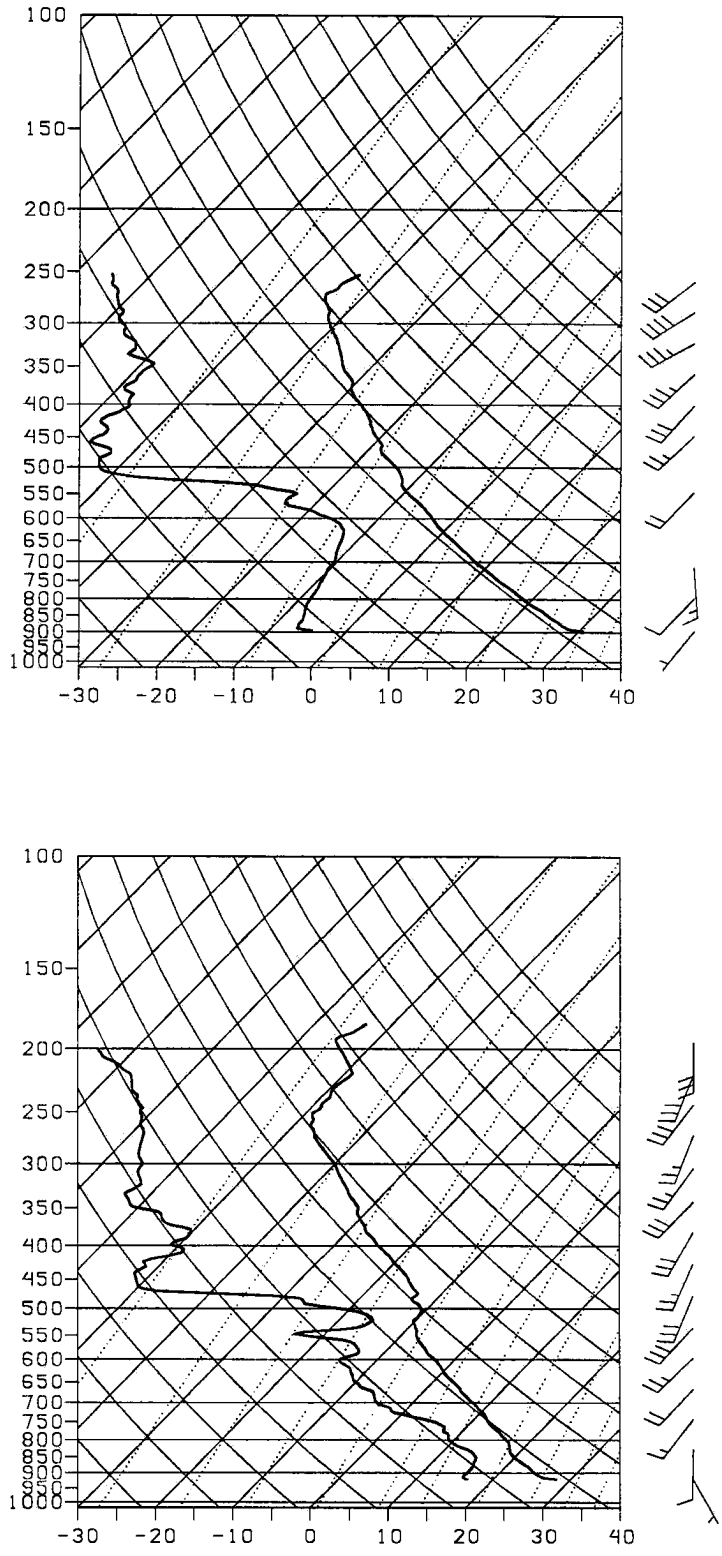

Figure 2.4: M-CLASS soundings from west of dryline (top) and east of dryline (bottom) around 2300 UTC.

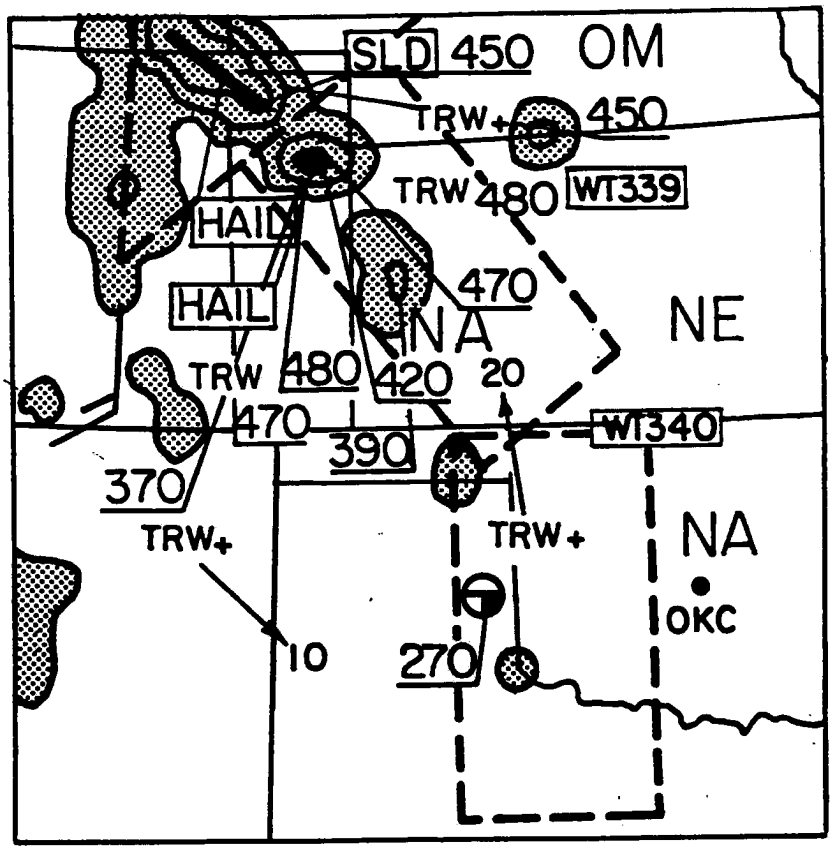

Figure 2.5: National Weather Service radar summary for 2235 UTC, 15 May 1991.

northern section of the dryline in southwest Kansas. By 2300 UTC, a few convective storms had developed in the eastern Texas Panhandle and begun moving northeast. Figure 2.5 shows a National Weather Service radar summary from 2235 UTC. Two of the storms which developed along the dryline eventually produced tornadoes near Laverne, Oklahoma and Shamrock, Texas that evening.

2.2 Model Configuration

2.2.1 General Information

The model employed for this study was the Colorado State University Regional Atmospheric Modeling System (CSU-RAMS, hereafter referred to as RAMS) described by Pielke et al. (1992). RAMS has been validated as a forecast tool for

various types of weather (e.g. Cram and Pielke 1987; Lyons et al. 1988; Cram et al. 1992; Papineau 1992; Cotton et al. 1994). For this study, it was configured as a three-dimensional, non-hydrostatic, fully compressible, primitive equation model. Surface layer fluxes were parameterized using a prognostic soil model (Tremback and Kessler 1985) and vegetation model (Avissar and Pielke 1989). Vegetation parameters such as albedo, roughness length, and Leaf Area Index (LAI) were specified based on the vegetation type. Vegetation type (or land-surface category) was specified as one of 18 possible values based on the Biosphere-Atmosphere Transfer Scheme (BATS, Dickinson et al. 1986). Turbulence and diffusion parameterizations were handled using the Smagorinsky deformation K method with a dependence on the local Richardson Number.

To resolve some of the finer scale features of the dryline environment, a nested grid configuration employing an Arakawa-C nesting scheme was used. Figure 2.6 shows the grid configuration used for all simulations in this paper. Table 2.1 contains information for each of the grids. The model utilized 40 vertical atmospheric grid points. The minimum vertical spacing at the lowest level was 100 m, and was stretched exponentially to a maximum of 1000 m throughout a vertical domain of approximately 18 km. The top boundary was specified as a rigid lid with the top four grid points nudged towards observed conditions to act as an absorber of gravity waves. A terrain-following vertical coordinate was employed. In the soil model, 11 vertical levels with an average spacing of 4 cm was used. A microphysical parameterization for warm rainwater formation was used. Mean droplet diameter was specified from a default value in the model code. The number concentration of raindrops was then diagnosed from the prognosed mixing ratio and the specified droplet diameter. As configured, the model required approximately 60 hours of CPU time per 12 hours of simulated time while running on an IBM RISC-6000, 371-series workstation. All simulations were run from 1200 UTC, 15 May 1991, to 0000 UTC, 16 May 1991.

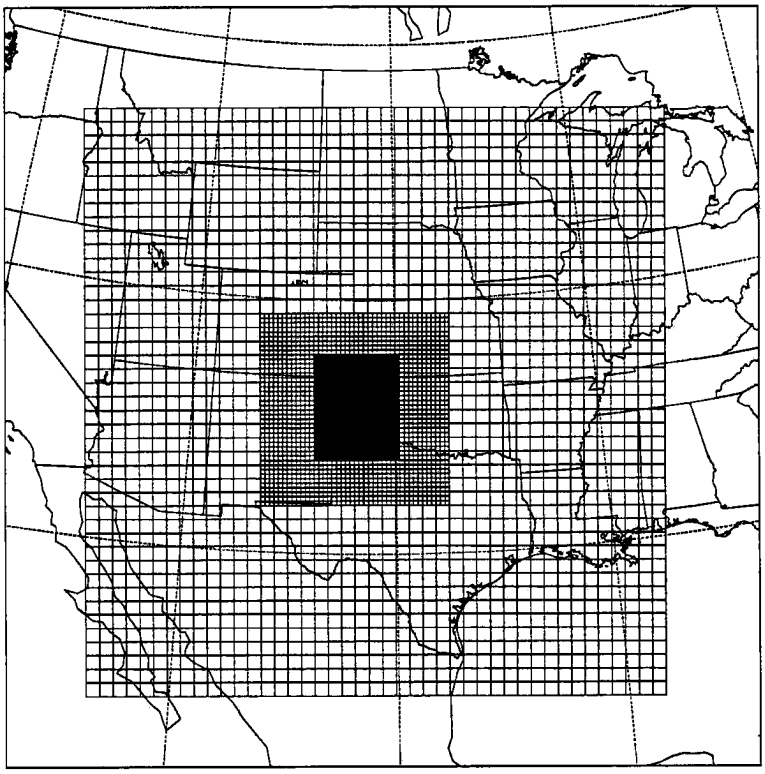

Figure 2.6: RAMS nested grid configuration for all simulations in this study.

Table 2.1: Model Grid Specifications

Grid	ΔX (km)	No. of X Points	No. of Y Points	Timestep(s)
1	60	45	45	90.0
2	20	44	44	30.0
3	5	78	94	7.5

2.2.2 Initialization of the Control Simulation

Atmospheric variables were initialized using a combination of gridded 2.5 degree NMC pressure data, upper air soundings, and surface observations for 1200 and 0000 UTC. The data were obtained from the mass storage system at NCAR. Lateral boundary conditions for the outer 5 grid points on the coarse grid were provided by a linear time series created from the data mentioned above ("nudging").

Topography, vegetation type, land percentage, and sea surface temperature were read onto the grids from USGS datasets which have been configured for use in RAMS. Plots of the topography and vegetation type on the fine grid are shown in Figures 2.7 and 2.8. For this simulation, the vegetation types on grid 3 were crop/mixed farming (1), short grass (2), evergreen needle leaf tree (3), irrigated crops (10), and evergreen shrub (16).

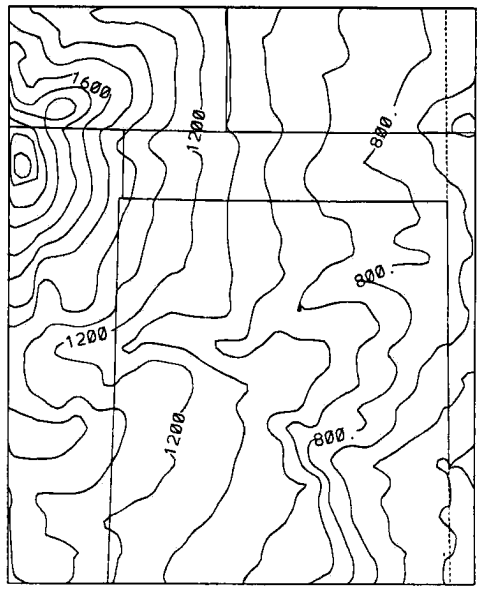

Figure 2.7: Topographic contours (m) on grid 3. Contour interval is 100 m.

As mentioned earlier, LAI is a function of the vegetation type. It is also a function of the seasonal average surface temperature. During the month of May, the vegetation in the Great Plains is near maximum "greenness", so the LAI is also approaching a maximum. In the BATS model the value of maximum LAI for

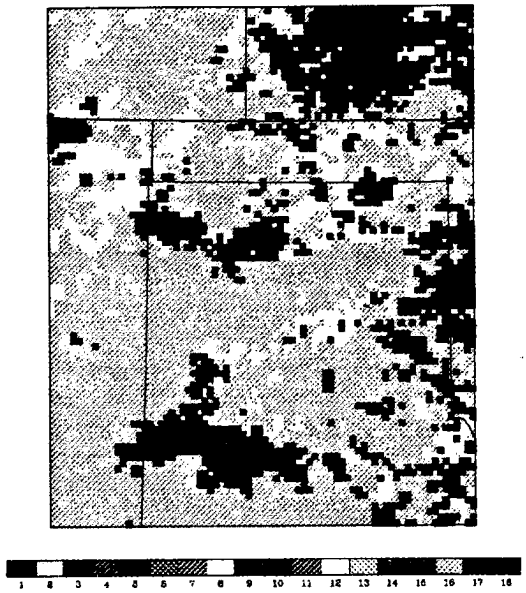

Figure 2.8: Land cover and vegetation type from the Biosphere-Atmosphere Transfer Scheme (BATS; Dickinson et al., 1986) on grid 3. Predominant vegetation types on this grid are (1) crop/mixed farming; (2) short grass; (3) evergreen needleleaf tree; (10) irrigated crop; and (16) evergreen shrub.

all vegetation types other than short grass, which has a maximum value of 2.0, is 6.0. Preliminary tests showed surface fluxes were much higher than what one would expect, based on measurements of surface fluxes for similar conditions (e.g., Stull 1988). Following Avissar and Pielke (1989), the contribution to the surface fluxes by the vegetation canopy is directly proportional to the LAI. A factor of two is also included in this modification to account for both sides of the leaves contributing to the heat fluxes. This led to the question of whether the values of LAI specified in BATS were appropriate, or if the simple linear relationship between LAI and the vegetation contribution to the turbulent fluxes used in the model was representative.

Lee (1992) calculated LAI directly from NDVI data for the northern Great Plains for May 1990. His results are shown in Figure 2.9. Note that none of the LAI values calculated from the satellite data exceed 2.0 anywhere on his grid. Consideration of the Beer-Bougher law suggests that although the actual LAI may be as high as 6.0 or more, the amount of light reaching leaves at the bottom of the canopy will be greatly reduced, thus decreasing transpiration by these inner leaves. Therefore,

Figure 2.9: LAI distribution over the central Great Plains for May 1990 (after Lee 1992). Contour interval is 0.2.

the "effective LAI" in terms of enhancing the surface flux will be reduced. Lemeur and Rosenberg (1979) used their SHORTWAVE model to predict the reflectance of total shortwave, near infrared, and photosynthetically active radiation (PAR) as a function of LAI and sun angle over a poplar forest. They concluded that the effect of LAI on transpiration is insignificant after a value of 2 is achieved. Based on these findings and the apparently unrealistically high fluxes, test runs were made with the LAI limited to 3.0 or less in the surface flux calculations. If the specified vegetation type had an LAI exceeding 3.0, the value was set to be equal to 3.0. If the specified LAI value was less than or equal to 3.0, then the actual value was used. This scheme produced realistic values of sensible and latent heat fluxes, and also gave the best results with respect to the observations of surface meteorological parameters. Thus, it was decided that the control simulation would employ this modification to the RAMS code. A sensitivity test simulation which did not limit LAI (standard configuration) is described in Chapter 3.

An antecedent precipitation index (API) was used to initialize the soil moisture for the control simulation (Wetzel and Chang 1988). An API value was calculated for each reporting station from a three month series of 24-hour precipitation data and included a parameterization of bulk evapotranspiration. The API values were then converted into a value of volumetric soil moisture for sandy clay loam and objectively analyzed using a Barnes scheme. This analysis was then interpolated onto the RAMS grids. To ensure that the API was a realistic representation of the conditions, the analysis was confirmed by comparing it to the Weekly Crop Moisture Index for 11 May 1991 (USDOC/USDA 1991). Figure 2.10 shows the volumetric soil moisture analysis on Grid 2.

2.3 Control Simulation Verification

In order to lend credibility to any sensitivity tests, it is vitally important to show that the CONT simulation reasonably approximated the observed conditions. The

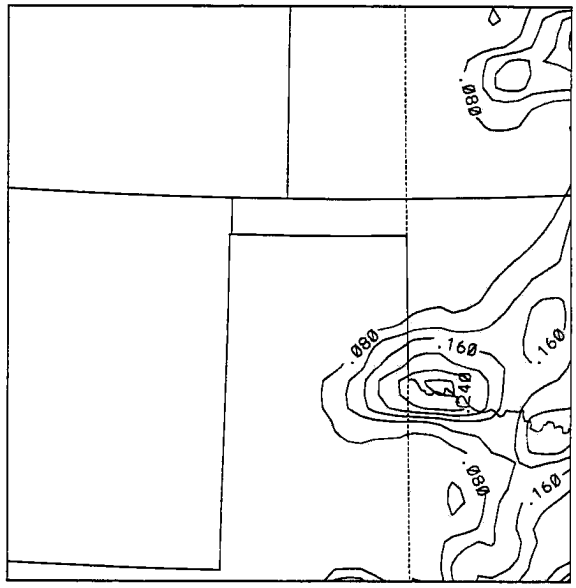

Figure 2.10: Volumetric soil moisture distribution on grid 2 for the CONT simulation. Values represent fraction of total moisture capacity of the soil.

CONT run did an excellent job of depicting the location, orientation, and structure of the observed dryline.

Results from the second grid will be used for the horizontal cross section plots, since for verification purposes the 20 km grid spacing is broadly comparable to the finest surface station spacing. Additionally, the NWS and PAM-II observations have been interpolated to a grid with the exact same coordinates and projection as the model's grid 2 and analyzed with a Barnes objective analysis. Figures 2.11 and 2.12 show a comparison of surface temperature and surface mixing ratio at 0000 UTC, respectively. Both plots also include the wind vectors. One should note that the gradients of temperature and moisture as analyzed from the observations may not reflect the strength of the actual gradients due to coarse horizontal spacing of the observations.

The isotherm plots reveal that the CONT run simulated the pattern and magnitude of the isotherms rather well. The positions of the warm tongue over the Texas Panhandle and the cold front over eastern New Mexico are correct, although the cold front does appear to be oriented more north to south in the simulation

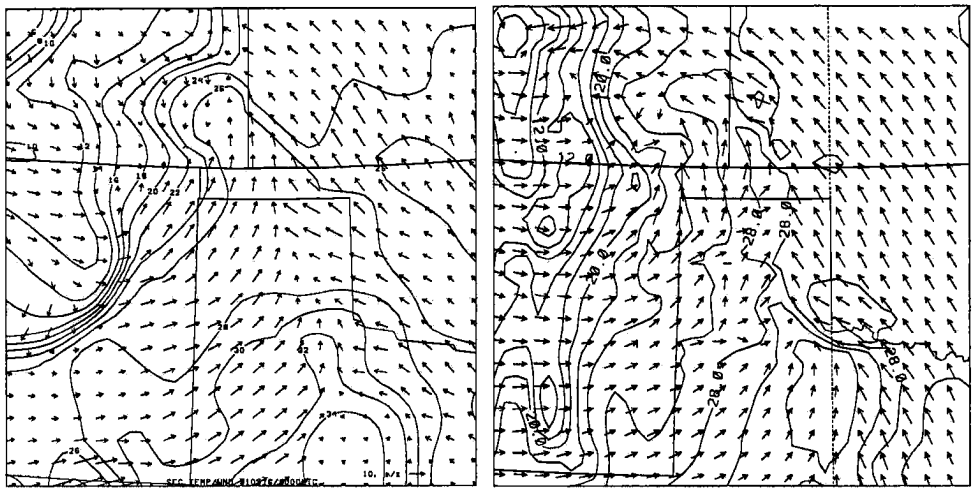

Figure 2.11: Objective analysis of temperature (contour interval of 2°C) and wind vectors as observed (left) and for the CONT simulation (right) at 0000 UTC, 16 May 1991. Vectors are of similar scale on the two plots. A reference vector is included in the lower right corner of the left panel.

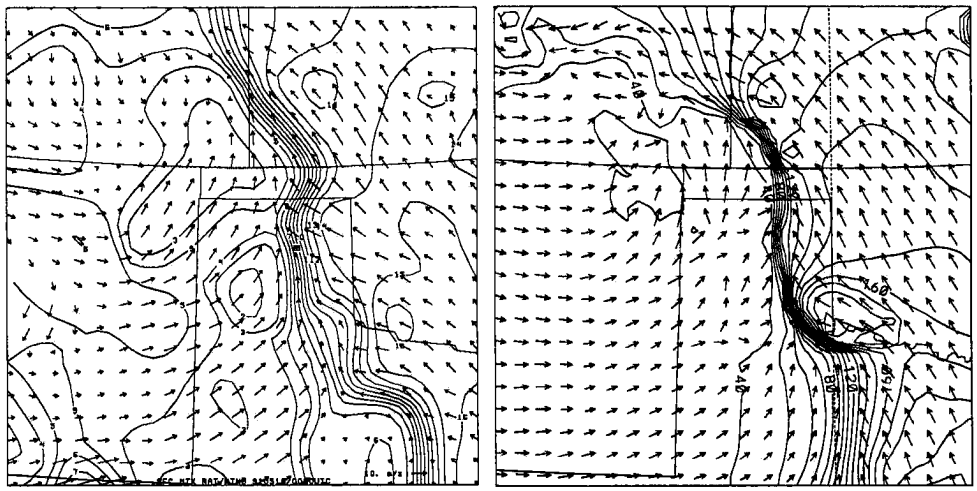

Figure 2.12: Same as 2.11, but for water vapor mixing ratio (contour interval of 1 g kg^{-1}).

than observed. Although the 28°C isotherm does not extend into the Oklahoma Panhandle on the observation analysis as it does in the simulation, there were stations reporting temperatures of 28°C in that region (see Figure 2.2). The smoothing of the Barnes analysis scheme tends to miss narrow features, and the model results seem to indicate that the zone of 28°C temperatures along the warm tongue was fairly narrow. The cool pocket of 26°C temperatures over southwest Oklahoma in the simulation does not appear as obvious on the analysis of the observations. However, if one again refers back to Figure 2.2, there was a band of cooler temperatures (26°C) extending northwest from southwest Oklahoma.

Comparison of the surface mixing ratio fields also indicates the high quality representation of observed conditions by the CONT simulation. If one arbitrarily chooses the 7 g kg^{-1} isohume to represent the approximate location of the dryline, it becomes obvious that the model reproduced the location and shape of the dryline almost identically. The moisture gradient in the simulation is much sharper than the objective analysis, presumably due to the smoothing of the Barnes analysis. In actuality, based on the M-CLASS soundings and the aircraft traverses, the simulated moisture gradient is actually *slightly less* than observed. If a finer grid had been employed (e.g., 1 km spacing), gradients as intense as the actual moisture gradient probably would have developed. However, the simulation is still able to resolve features that could not have been observed from the standard observational data.

The main discrepancy in the simulation concerning the moisture field is that the model tends to be too moist, both east and west of the dryline. The moist patch over southwest Oklahoma (which corresponds to a moist patch of soil) is 2 to 3 g kg^{-1} too moist in the simulation and covers a larger area than the observations would indicate. Horizontal flow is devergent over the moist patch, suggesting the development of a Non-Classical Mesoscale Circulation or NCMC (Segal and Arritt 1992). West of the dryline, the simulation results are very comparable to the observations with the

exception of the west-central Texas Panhandle where a patch of extremely dry air was apparent in the observations. This may be a result of the initial conditions being to moist due to the coarse vertical resolution of the NMC analysis and the coarse horizontal spacing of NWS upper air soundings. Overall, the reproduction of the pattern and gradient is as good as expected from a numerical simulation using current 1995 modelling tools.

As with the surface temperatures and mixing ratios, the CONT run also simulated the winds with accuracy. The position of the circulation center associated with the low pressure system in southeast Colorado was predicted accurately, as well as the zone of confluent winds associated with the dryline. One important feature which appears in both the observations and the CONT simulation is the zone of nearly easterly winds in extreme southwest Oklahoma extending about 50 km south into Texas. This area of strong ageostrophic easterly winds corresponds to the area of extremely moist soil in the model initialization. If these easterly winds are a result of solenoidal forcing induced by the soil moisture gradient, one might presume that the soil moisture analysis created by the API method was representative.

The following comparisons will utilize individual station information from both National Weather Service and PAM-II sites, M-CLASS soundings, and data collected from the P-3 traverses. Figure 2.13 shows the locations of these various data sources.

Figure 2.14 shows soundings derived from the CONT run output corresponding to the same time and locations as the M-CLASS soundings shown in Figure 2.4. The soundings exhibit the classical features of the west and east dryline environments and strongly resemble the observed soundings for this particular case. The slight cool, moist bias of the simulation is noticeable in the eastern sounding. This results in the inversion being slightly lower and more pronounced than the observed sounding. The western sounding simulated the temperature profile with accuracy but it is also slightly too moist compared to observations. This may be a result of the initial

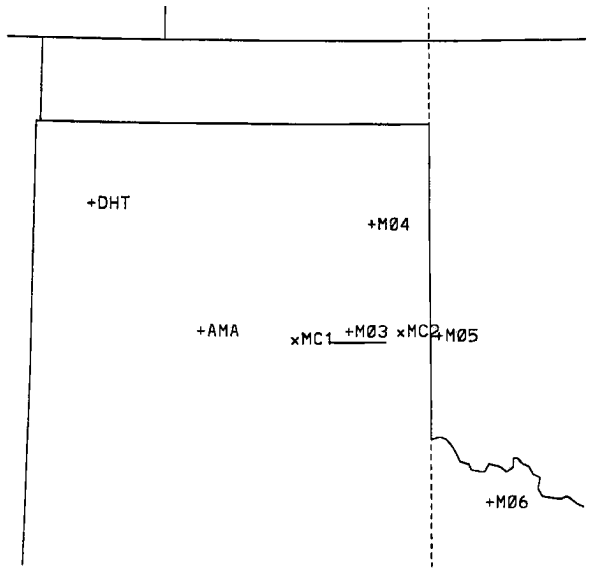

Figure 2.13: Locations of data sources used for single-point and vertical cross-section comparisons of the CONT simulation to observations. MC1 and MC2 represent the M-CLASS sounding locations at 2300 UTC. The horizontal line segment near the soundings shows the location corresponding to the cross section in Figure 2.3.

conditions being too moist due to the coarse vertical spacing of the NMC analysis and the coarse horizontal spacing of NWS soundings.

Various parameters calculated from the soundings are compared with observed values in Table 2.2. The thermodynamic indices were calculated based on an average of the lowest 1 km conditions. The storm-relative helicity (SREH) was calculated for the surface to 4 km layer. An estimated storm motion was calculated for each grid point by taking 75 percent of the mean 3-10km wind speed and adding 30° to the mean direction (i.e., storm motion slightly to the right).

Figure 2.15 shows vertical cross sections of mixing ratio and vertical motion from grid 3 at 0000 UTC on a horizontal scale identical to Figure 2.3. Because the simulated dryline was approximately 30 km farther west than the observed location along this transect, the model cross section was taken 20 km farther west than shown in Figure 2.13 in order to have the entire dryline visible on the plot. The error in forecast location is rather insignificant, considering possible error in the P-3 analysis mentioned earlier and the tendency of drylines to have waves and bulges along their

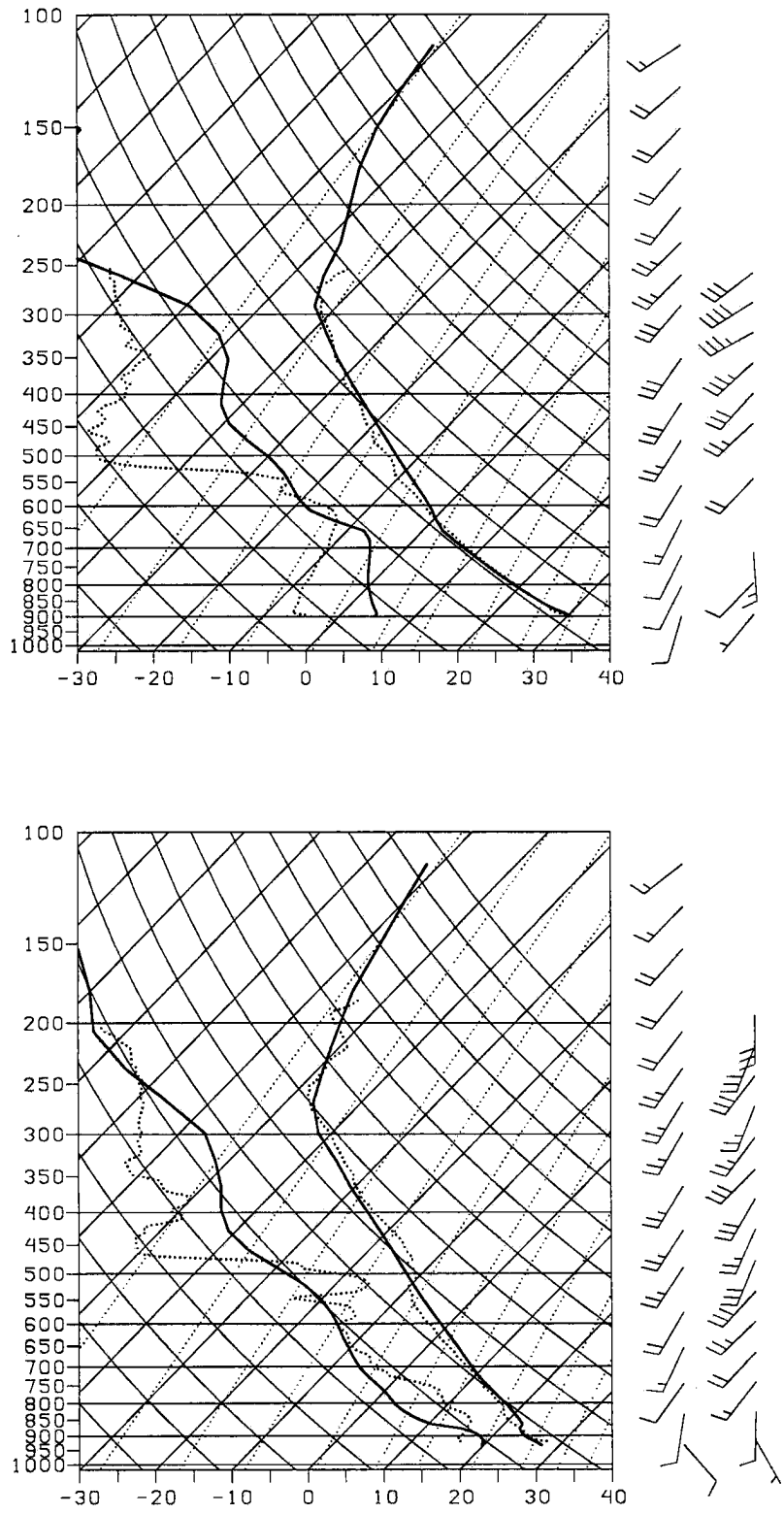

Figure 2.14: Skew-T plots of temperature (C) and dewpoint (C) for MC1 (top) and MC2 (bottom). Solid lines are from CONT run closest grid point. Dotted lines are the observed profiles. Left and right wind profiles are from the CONT run and observations, respectively. Winds in m s^{-1}.

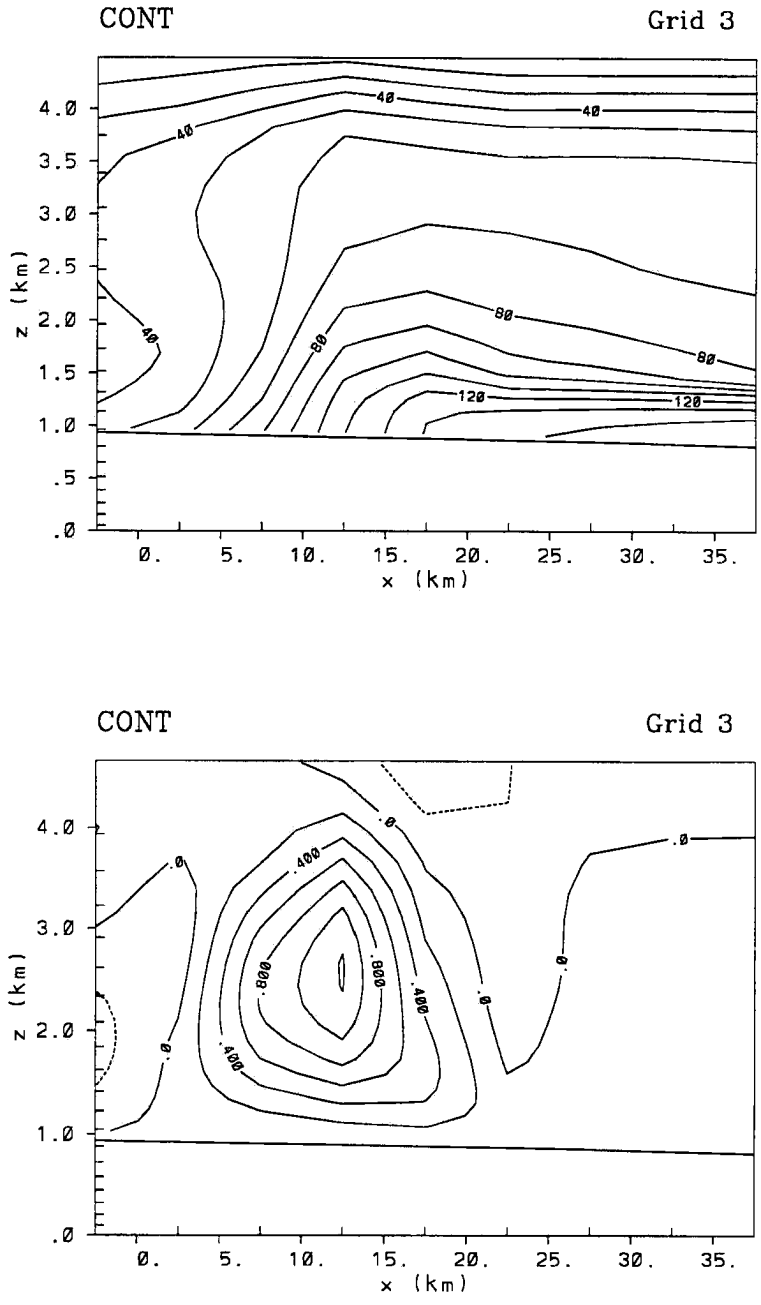

Figure 2.15: Vertical cross sections from the CONT run at 0000 UTC for a transect shifted 20 km from the transect depicted in Figure 2.13. The top panel is an analysis of water vapor mixing ratio (dg kg^{-1}), and the bottom panel is for vertical motion (m s^{-1}).

Table 2.2: Comparison of observed and CONT simulation sounding parameters for 2300 UTC, 15 May 1991. Thermodynamic variables were calculated based on mean conditions of the lowest 1 km. SREH is calculated from 0-4 km.

	Mean Temp for lowest 1 km (°C)	Mean Mixing ratio for lowest 1 km (g kg^{-1})	Convective Temp (°C)	Lifted Index (°C)	CAPE (J/kg)	SREH (m^2s^{-2})
Obs. West	23.7	2.6	30.6	1.9	0	−6.5
CONT West	23.8	5.3	30.4	−1.5	251	71.3
Obs. East	21.7	12.4	29.1	−6.9	1839	176.5
CONT East	22.9	10.9	30.7	−6.5	1780	175.5

length which may be imperfectly simulated. Such waves and bulges affect the exact location of any small segment (e.g., Koch and McCarthy 1982).

The observed strength of the surface mixing ratio gradient across the dryline was slightly higher than the modelled gradient. The CONT simulation produced a surface mixing ratio gradient of 0.5 g kg^{-1} km^{-1}, about 0.1 g kg^{-1} km^{-1} lower than the observed gradient. The maximum vertical motion is also lower in the CONT simulation, with a peak value of 1.2 m s^{-1} versus the observed updrafts exceeding 2.5 m s^{-1}. The slightly weaker moisture gradient and vertical velocities can probably be attributed to the resolution of the fine grid which is probably not adequate to form such strong, narrow gradients (Ziegler et al. 1995). As previously mentioned, the environment east of the dryline appears to be a little too moist in the CONT simulation compared to observations, which results in a slightly lower predicted boundary layer height. The location of the peak updraft with respect to the moisture gradient and height above ground was predicted very accurately, as was the bulge of moisture co-located with the peak updraft. As in the case of previous comparisons, the model did an overall good job of reproducing the observed conditions.

One tool which can be used to determine how well the model represented the partitioning of the sensible and latent heat fluxes is the conserved variable diagram. Following Betts (1982, 1984), and Ziegler and Hane (1993), time series plots of mixing ratio versus potential temperature at the surface were plotted for several

stations east and west of the dryline and compared to model results. These time series plots represent "mixing lines". The slope of these lines provide an indication of the Bowen Ratio. Similar slopes between the modeled and observed mixing lines would indicate that the model provided a reasonable representation of the surface flux partitioning. The advantage to using this method is that it is relatively insensitive to differences between the model and observations at the initial time.

Figure 2.16 contains plots for four PAM-II stations located east of the dryline and corresponding plots from the nearest grid location in the CONT simulation. Again, in all cases except at station M06, the model results were slightly too moist. This difference is most pronounced at stations M03 and M05 in the late afternoon hours. The profile at M03 together with the P-3 traverses (not shown) that the dryline reached this station from the west around 2200 UTC, as entrainment drying occurred from 1500 to 2200 UTC, with some of the drying possibly offset by horizontal transport of moisture from 1600 to 1700 UTC. From 2200 to 0000 UTC, it appears as if the dryline retreated back to the west of the station. There was a much weaker indication of warming and drying at this location in the CONT simulation, and the modelled drying occurred later in the day, from 1900 until 2200 UTC. It was pointed out earlier that the simulated dryline was approximately 30 km to the west of the observed location. This would probably account for the discrepancy at station M03, which apparently was very near the dryline throughout the afternoon hours. At M05, the model results showed moistening continuing until 2000 UTC, while the observation indicated a generally constant amount of moisture from 1600 until 2000 UTC. After 2000 UTC, the atmosphere warmed and dried until 2300 UTC, and the model captured this feature fairly accurately. The other two stations appear to have been modeled reasonably well. All four stations reflect characteristics of "moistening" or "entrainment-drying" convective boundary layers (Mahrt 1991), with the westernmost stations moving from the moistening to drying phase earlier than the easternmost stations.

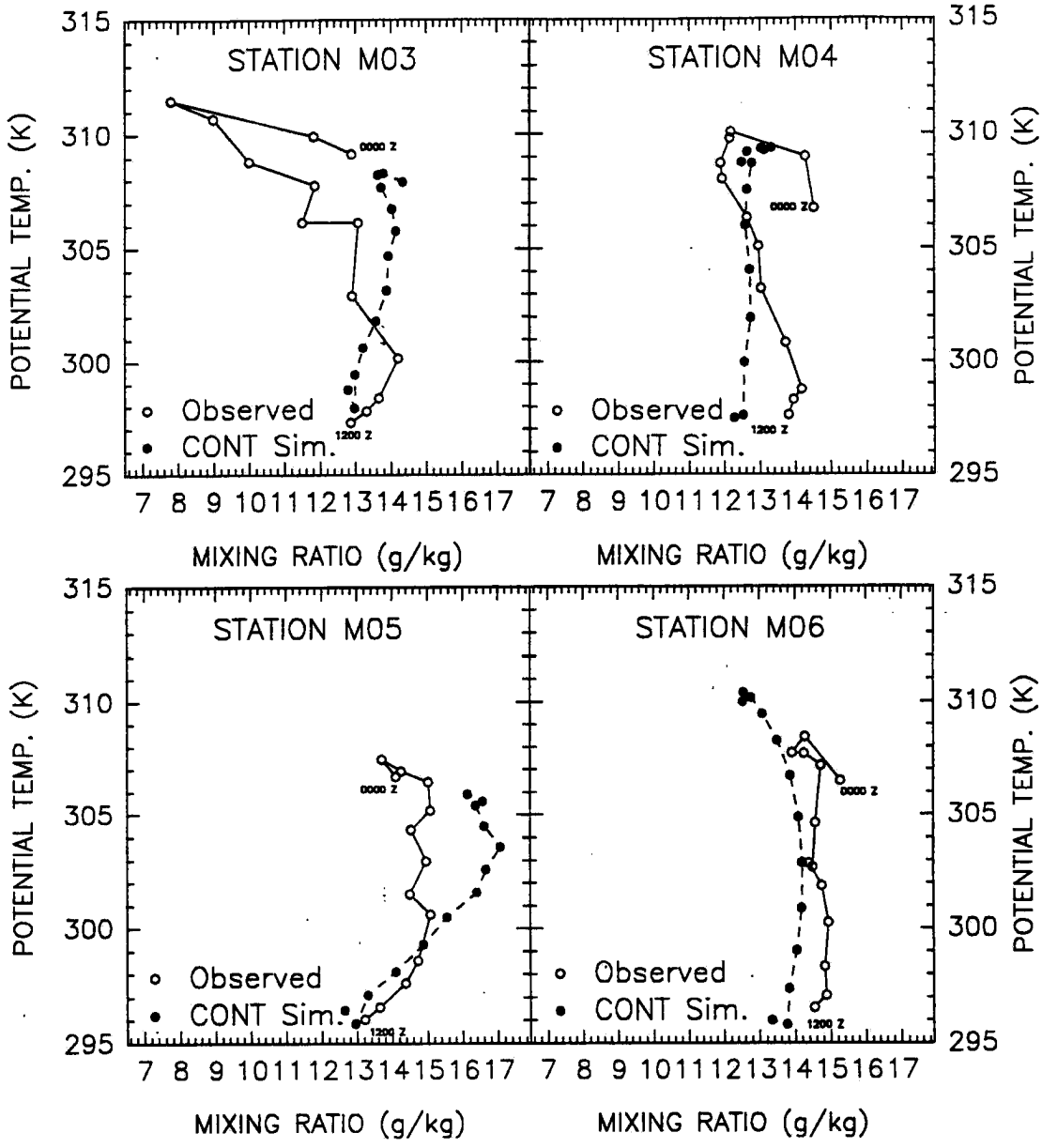

Figure 2.16: Conserved variable time series diagrams for four observation sites east of the dryline comparing observations to model grid point data.

Figure 2.17 contains the same type of plot as Figure 2.15 for Dalhart and Amarillo, both of which were west of the dryline throughout most of the day. The mixing lines for both stations were modeled very accurately and indicate the warming and drying trend that one would expect for locations west of a dryline. Strong entrainment warming and drying at AMA from 1400 to 1500 UTC, indicative of dryline passage, was not emphasized in the model, although a wind shift and diffuse moisture gradient was simulated. Inspection of P-3 data (not shown) indicates that the dryline was 15-30 km east of AMA around 1530 UTC. The strong drying observed at AMA from 1400 to 1500 UTC is indicative of the dryline inversion being eroded.

A plot of the sensible and latent heat fluxes is shown in Figure 2.18. The location of the moist patch of soil in southwest Oklahoma is very obvious on these plots. The sensible heat flux actually decreases to 0 W m^{-2} or less in this area, while the latent heat flux exceeds 400 W m^{-2} and approaches 500 W m^{-2}. The result is a gradient of sensible and latent heat fluxes with opposite signs of approximately 225 W m^{-2} (50 km)$^{-1}$ in the southern portion of the Texas Panhandle. This value is about twice the value that Ziegler et al. (1995) determined to be required for dryline formation. Since the value here is a peak value and not a north-south average, this result is comparable to their results. The strong gradient of latent heat flux no doubt contributes to the intensification of the atmospheric moisture gradient in this region. The strong gradient in sensible heating provides a mechanism through which thermal gradients are produced, which may induce mesoscale circulations in this region that work to further intensify the atmospheric gradients (Pielke and Segal 1986). Referring back to Figures 2.11 and 2.12, one can see that strong gradients of temperature and moisture existed in the area of the flux gradient in both the observations and the simulation. Additionally, there was an area of winds with more of an easterly component just to the east of the flux gradient both in the observations and simulation.

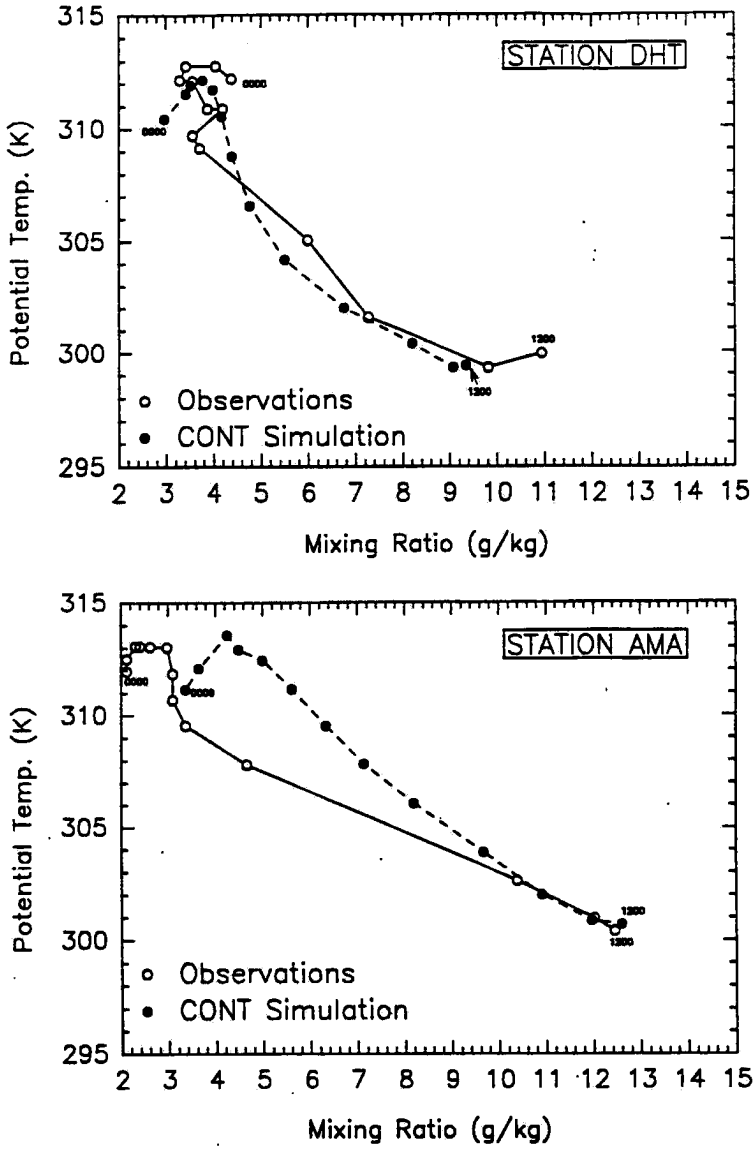

Figure 2.17: Same as 2.16 but for two stations west of the dryline.

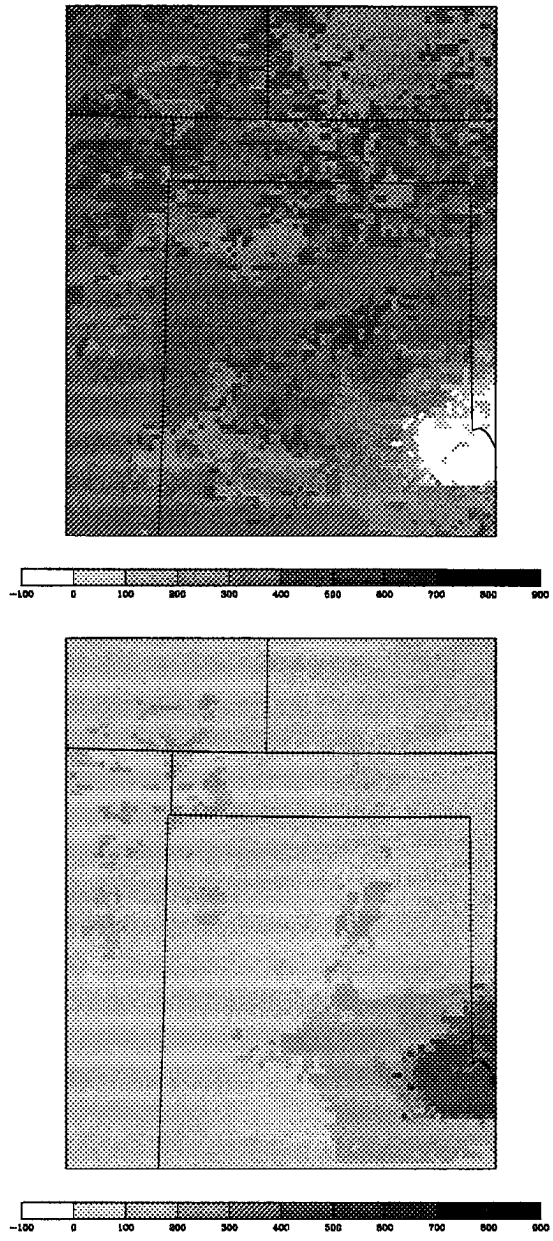

Figure 2.18: The sensible (top) and latent (bottom) heat fluxes (W m^{-2}) on grid 3 from the CONT run at 2000 UTC.

The fine grid used in the simulation was not of high enough resolution in order to explicitly resolve convection. Nevertheless, the model produced local regions of grid-scale water saturation due to lifting of moisture at the dryline. It is still of some interest to view the areas of "resolved" precipitation due to so-called "pseudo-convection", which are related to but distinct from parameterized sub-grid convection. Figure 2.19 is a plot of accumulated total precipitation for the duration of the simulation. The model produced rain in the same region where the deepest convec-

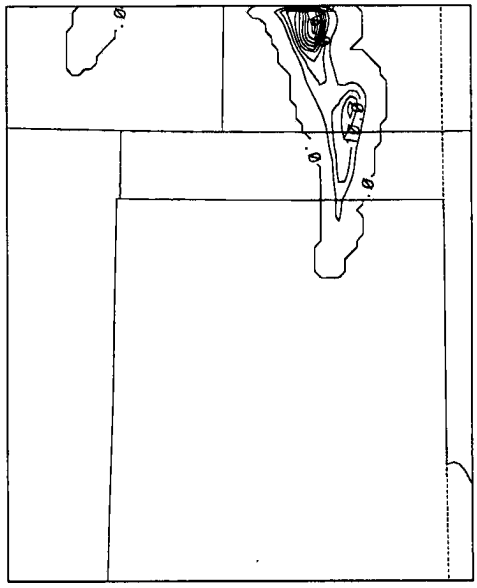

Figure 2.19: Total accumulated precipitation (mm) on grid 3 for the CONT simulation.

tion associated with the dryline was observed, in southwest Kansas, the Oklahoma Panhandle, and the extreme northern portion of the Texas Panhandle. No precipitation was produced by the model in the central Texas Panhandle where convection was indicated by the radar summary in Figure 2.5. These cells were smaller and hence probably could not be represented using a 5 km grid spacing. These results are broadly comparable to Lakhtakia and Warner (1987), who employed a sub-grid convective parameterization to simulate formation of "lid-edge" precipitation using the Pennsylvania State MM4 regional model. Due to the much finer grid resolution

in the present case, precipitation is much more localized and produces more realistic low-level cold pool boundary layer features than in the MM4 simulation study.

Overall, the quality of the CONT simulation is quite impressive. Following the methodology utilized by Keyser and Anthes (1977) and outlined by Pielke (1984), values of model RMS error (E), unbiased RMS error (E_{ub}), and the standard deviation of the observations (σ_{obs}) and closest model grid points (σ) were computed for each hour of the CONT simulation. The six stations used for the analysis were AMA, DHT, M03, M04, M05, and M06 (see Fig. 2.13). The ratios of σ/σ_{obs}, E/σ_{obs}, and E_{ub}/σ_{obs} are shown for surface potential temperature and surface mixing ratio in Tables 2.3 and 2.4, respectively. Also included in these tables is the model bias, which was calculated by subtracting the mean value of the observations from the mean value of the corresponding model grid points. For a model to have skill, the first ratio should be near unity, while the second and third ratios should be less than one. The smaller the latter two ratios are, the better the skill indicated. Although an entire grid cannot be completely evaluated by only six observations, the results for the CONT simulation are very encouraging. It is especially encouraging because data from the four PAM stations used in this analysis were not included in the model initialization. It should also be noted that small errors in temporal and spatial displacement of the modelled fields can result in poor verification, even if the model predicts the pattern exactly (Pielke 1984).

The tables confirm that the model exhibited a cool, moist bias compared to the observations. It is interesting to note that at the intial time, the model actually had a warm, dry bias. The shift to a cool moist bias later in the run suggests that the simulated latent heat flux may have been slightly too high, thus implying a higher Bowen Ratio than what was observed. This is supported by the saturation point diagrams shown earlier.

Because RAMS has shown the capability to accurately predict the evolution of the dryline for this particular case, sensitivity tests can be used to determine

the impact of various parameters on the dryline. The tests performed for this research involved the soil moisture and vegetation effects and are described in the next chapter.

Table 2.3: Ratios indicating CONT run skill for 6 point observations of surface potential temperature. Bias values are in degrees K.

Time	σ/σ_{obs}	E/σ_{obs}	E_{ub}/σ_{obs}	Bias
12Z	0.99	0.43	0.42	0.16
13Z	0.81	0.46	0.34	-0.44
14Z	1.09	0.51	0.50	-0.18
15Z	1.66	0.67	0.55	-1.21
16Z	1.53	0.76	0.53	-1.87
17Z	1.33	0.66	0.48	-1.49
18Z	1.29	0.52	0.49	-0.64
19Z	1.06	0.52	0.50	-0.47
20Z	0.90	0.44	0.40	-0.54
21Z	0.84	0.69	0.65	-0.55
22Z	0.91	0.77	0.74	-0.46
23Z	0.99	0.66	0.64	-0.34
00Z	1.32	0.80	0.80	0.11
MEAN	**1.13**	**0.61**	**0.54**	**-0.62**

Table 2.4: Same as Table 2.3 but for surface mixing ratio. Bias values are in g kg^{-1}.

Time	σ/σ_{obs}	E/σ_{obs}	E_{ub}/σ_{obs}	Bias
12Z	0.86	0.94	0.61	-0.82
13Z	1.09	0.52	0.28	-0.73
14Z	1.43	0.38	0.33	-0.49
15Z	1.61	0.51	0.50	0.38
16Z	1.44	0.43	0.38	1.04
17Z	1.24	0.37	0.29	1.11
18Z	1.09	0.37	0.28	1.13
19Z	1.03	0.36	0.25	1.24
20Z	1.02	0.44	0.33	1.46
21Z	1.02	0.47	0.36	1.52
22Z	0.99	0.56	0.45	1.61
23Z	1.00	0.34	0.34	0.37
00Z	0.99	0.38	0.38	-0.17
MEAN	**1.14**	**0.47**	**0.37**	**0.59**

Chapter 3

SENSITIVITY SIMULATIONS

3.1 Soil Moisture Sensitivity Tests

Two simulations were performed to evaluate the sensitivity of the modeled dryline to variations in the initial soil moisture field. The first (50SM) was initialized with the same API-derived variable soil moisture field as the CONT run but with all values reduced by a factor of 0.5. The second simulation (HOMD) was initialized with a homogeneous soil moisture field, in which an extremely dry value of volumetric soil moisture of 0.04 was specified over the domain. With the exception of the soil moisture initialization, the model configuration was identical to the CONT simulation for both of these sensitivity runs.

3.1.1 The 50SM Simulation

A plot of the soil moisture field for this simulation is shown in Figure 3.1. The net effect is a reduction of the soil moisture gradient in the vicinity of the dryline by 50 percent, as well as a reduction of the maximum available soil moisture across the patch in extreme southwest Oklahoma. The expected effect is a reduction of the latent heat flux in southwest Oklahoma, resulting in an increased sensible heat flux in this area and an overall reduction of the flux gradients. Plots of the surface sensible and latent heat fluxes from the 50SM run at 2000 UTC in Figure 3.2 reveal that this indeed was the effect of reducing the soil moisture gradient.

The maximum latent heat flux occurred in the same location as the CONT simulation but was reduced from nearly 500 W m^{-2} to just over 300 W m^{-2}. Additionally, the area covered by the latent heat flux maximum was much smaller. The

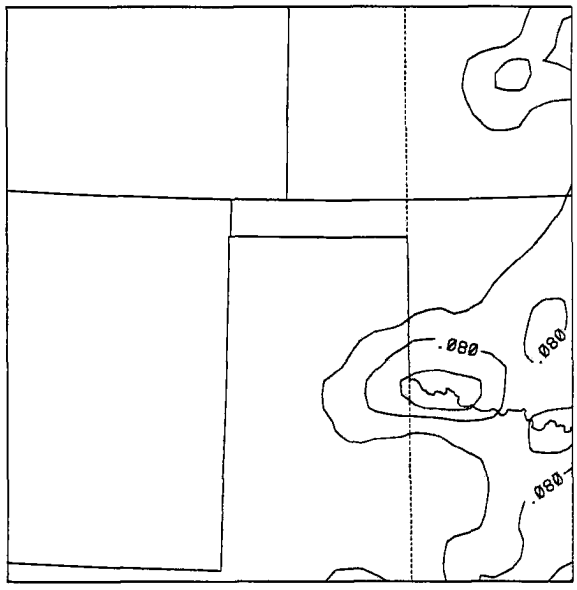

Figure 3.1: Volumetric soil moisture analysis 50SM simulation on grid 2. Contour interval is 0.04.

reduction in the sensible heat flux gradient appears to be directly proportional to the reduction of the soil moisture gradient, having been reduced from approximately 4.5 W m^{-2} km^{-1} to approximately 2.6 W m^{-2} km^{-1}. Since the moist soil appears to be a significant atmospheric moisture source, its reduction east of the dryline would be expected to reduce the moisture gradient at the dryline.

3.1.2 The HOMD Simulation

The HOMD results were very similar to the 50SM results, with differences not noticeable through qualitative inspection of many of the horizontal plots. Figure 3.3 shows the 2000 UTC surface fluxes of sensible and latent heat as computed in HOMD. There is still a slight gradient of sensible heat due to the higher atmospheric moisture content east of the convergence zone. The gradient of latent heat flux is no longer present in HOMD, due to the lack of any moist soil patches to provide additional moisture. Any moistening of the CBL in HOMD had to occur through horizontal advection. A north-south oriented maximum in latent heat flux is visible in the east-central Texas Panhandle. This maximum is probably due to horizontal

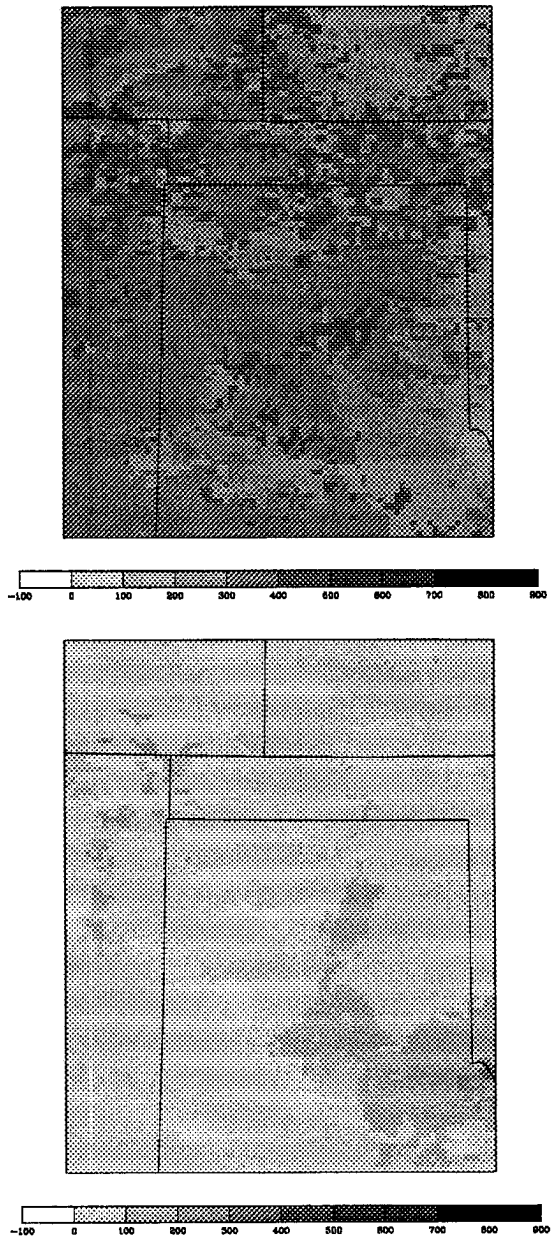

Figure 3.2: Sensible heat flux (top) and latent heat flux (bottom) at 2000 UTC from the 50SM simulation. Values are in W m^{-2}.

moisture flux convergence, as its location corresponds to an area of confluence in the wind field.

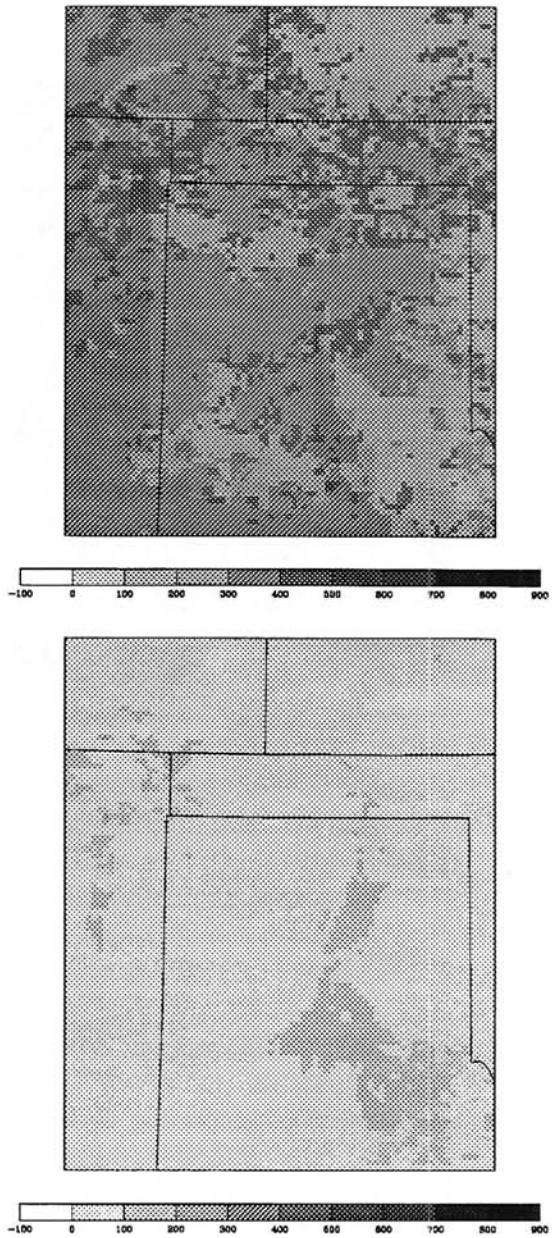

Figure 3.3: Same as 3.2 but for the HOMD simulation.

3.2 Vegetation Sensitivity Tests

Two simulations involving perturbations of the initial variable vegetation field specified in the CONT run were performed. The first (MLAI) utilized the same

variable vegetation field as the CONT simulation, but the model was run in its standard configuration. This allowed the LAI to be as high as 6.0 for all vegetation types except short grass, which has a maximum value of 2.0 in the BATS model. The second simulation (CVEG) utilized homogeneous vegetation. The vegetation type of short grass was specified for the entire domain. This vegetation type is most representative of the natural state of the grid 3 region, before agricultural and urban development. The goal of this simulation was to show the impact of using realistic variable vegetation, as well as possibly provide some insight as to how our modification of the land surface may have had an impact on regional climate.

3.2.1 The MLAI Simulation

The vegetation type specified for each grid point controls several variables used in the model. Surface albedo, roughness length, rooting depth, and LAI are all functions of the vegetation type. As mentioned earlier, the LAI was limited to a value of 3.0 or less in the CONT run for surface flux calculations. The standard BATS model employed in RAMS uses a maximum value of LAI and an annual variation for each vegetation type to determine the LAI for each vegetation type for the particular run. The value of LAI is determined as a function of the mean climatological surface temperature for the season and region of interest and is specified by the user. A value of 298 K for this temperature corresponds to maximum "greenness" in this scheme. This value was selected for use in the simulation, since the southern Great Plains region approaches maximum greenness in May and June (Loveland et al. 1991). Albedo, rooting depth, and roughness length were unchanged from the CONT simulation.

Since maximum greenness implies a seasonal maximum in LAI, most of the grid points in the domain of interest had an LAI of near 6.0. Wherever short grass was specified, however, the LAI only approached 2.0. This led to small patches having dramatic gradients in the surface sensible heat fluxes due to strong gradients

in the vegetation contribution to these fluxes. This could have a strong influence on the development of thermally forced circulations, provided vegetation patches are at least four times the grid spacing in width so that secondary circulations are adequately resolved.

Figure 3.4 shows the surface sensible and latent heat fluxes at 2000 UTC for this simulation. At first glance, the plots are very similar to the plots from the CONT simulation. However, closer inspection reveals that the MLAI simulation produced an even more heterogeneous field of surface fluxes, and that the typical values throughout the grid are much higher in many places by a difference in excess of 200 W m^{-2}. It was the initial examination of these fields that led to a suspicion that the parameterizations used for calculating the surface fluxes may not be physically representative. If the magnitudes of the fluxes calculated by the standard model are indeed overestimated, how does this effect the model's solution of the atmospheric conditions?

3.2.2 The CVEG Simulation

Since the use of variable vegetation provides for a large amount of heterogeneity of the surface conditions, the use of a constant vegetation type would presumably smooth the model results. The 2000 UTC flux plots from this simulation in Figure 3.5 reveal that this was the result. The sensible heat flux was nearly homogeneous with the exception of the areas of strong topographic gradients in New Mexico and Colorado, the dryline zone in the eastern Texas Panhandle, and the area of moist soil in the east Texas Panhandle and southwest Oklahoma. The latent heat flux is almost negligible on grid 3 except where the soil is moist. This graphically highlights the importance of the variable soil moisture. The area of maximum (minimum) sensible (latent) heat flux is actually much larger spatially and better defined in this simulation compared to all others because of the uniformity of roughness length, albedo, and LAI.

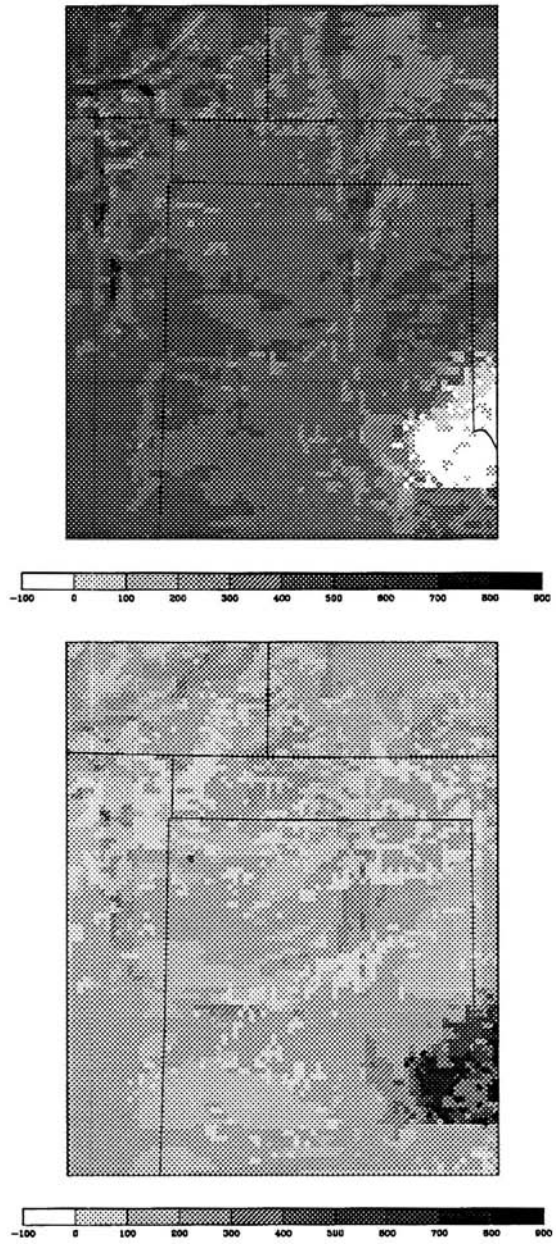

Figure 3.4: Same as 3.2 but for the MLAI simulation.

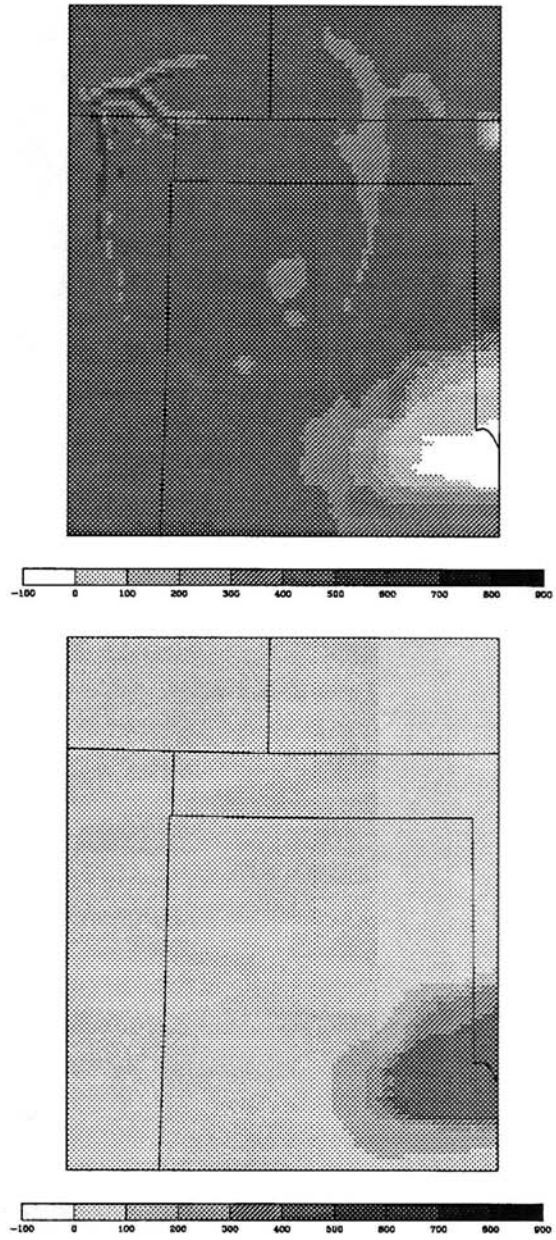

Figure 3.5: Same as 3.2 but for the CVEG simulation.

Chapter 4

RESULTS

It is apparent that variations in the soil moisture and vegetation directly impact the model's predicted sensible and latent heat fluxes. Changes in their values and the Bowen Ratio have a direct impact on the atmospheric thermodynamic and kinematic structure, thus affecting the morphology of the dryline. Using the CONT simulation as "truth", detailed comparisons to the sensitivity tests have been made using data from the finest grid. Since the spacing on this grid is 5 km, the effective resolution is approximately 20 km, which should be fine enough to resolve the coarsest features of the dryline. Additionally, some comparisons of the prestorm environment east of the dryline are made.

4.1 Dryline Structure and Morphology

4.1.1 Vertical Analysis

Although it is difficult to display three-dimensional results with two-dimensional information, Figure 4.1 gives a quick picture of how the dryline evolved in each of the simulations.

The plots contain the value of the water vapor mixing ratio from the lowest model grid point, averaged over 6 grid points oriented north to south, across an east to west transect of grid 3. The transect is centered on the same latitude as the P-3 cross sections shown earlier. The horizontal profiles are plotted at 3 hour intervals beginning at 1500 UTC for each of the simulations. In all five runs, the moisture gradient gradually formed and moved east until sometime after 2100

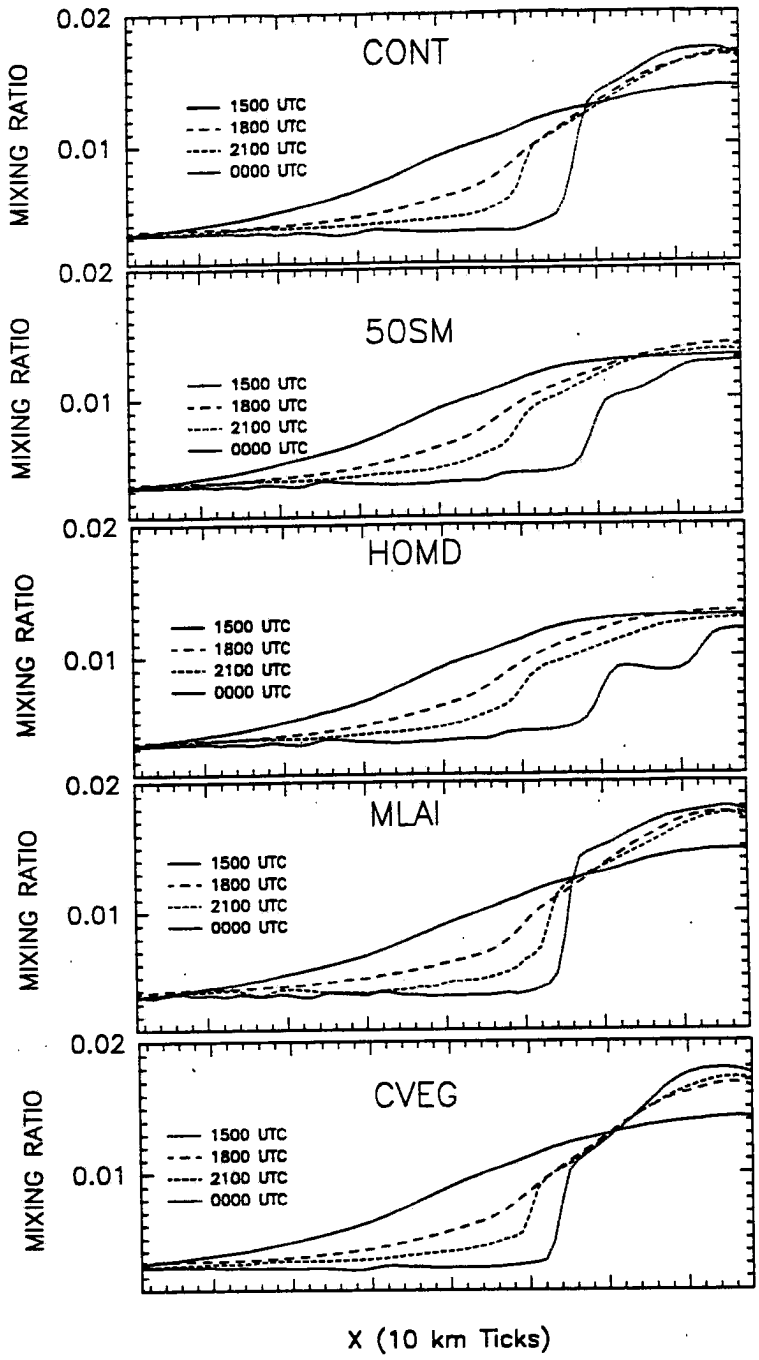

Figure 4.1: West to east profile of surface mixing ratio on grid 3 at 1500, 1800, 2100, and 0000 UTC for each of the simulations. Profiles are taken at same latitude as P-3 transect, averaging over 6 points in the north-south direction.

UTC. After 2100 UTC, the gradient sharpened dramatically and remained nearly stationary in the CONT, MLAI, and CVEG simulations. The gradient in the 50SM and HOMD simulations was much weaker and advanced farther east along this transect. Additionally, the CBL east of the dryline continued to moisten beyond the initial state during the afternoon hours in the CONT, MLAI, and CVEG runs. This continued moistening is supported by morning observations but was not observed during the afternoon. Drying of the CBL east of the dryline took place in the 50SM and HOMD runs. Apparently, the flux of moisture from the soil into the atmosphere played a key role in moistening the atmosphere and intensifying the gradient along the dryline. One additional point of interest is the double peak of moisture in the HOMD simulation. This multiple gradient feature has been observed in recent cases (Hane et al. 1993) and may be a manifestation of the breakdown of the vertical circulation east of the dryline into multiple circulations.

Figures 4.2 and 4.3 show a cross section analysis of the evolution of the dryline from the CONT simulation. The evolution of the dryline as depicted is consistent with the two-dimensional case study presented by Ziegler et al. (1995). At the model initialization time winds were westerly over the entire cross section with the exception of the extreme eastern and southern edge. A moist air mass existed across the eastern two-thirds of the grid, with decreasing depth to the west due to the increasing terrain height. The virtual potential temperature analysis at this time showed stable stratification, with a very subtle maximum at the surface located at the eastern edge of the moisture gradient. As the day progressed, the drier air to the west heated more rapidly than the moist air to the east. Hydrostatic pressure falls in the warmer air combined with a horizontal hydrostatic pressure gradient induced by the virtual temperature gradient to create a low-level easterly flow. As the western edge of the moist air continued to mix out, westerly momentum aloft was brought down to the surface. This enhanced the convergence along the dryline

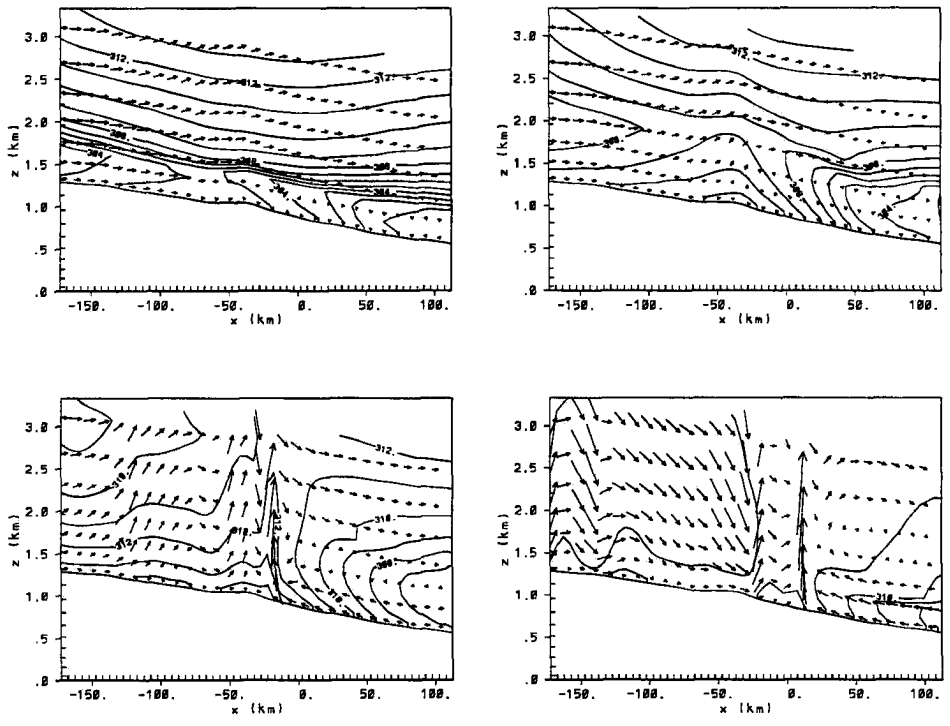

Figure 4.2: West to east vertical cross section of virtual potential temperature (K) on grid 3 at 1500, 1800, 2100, and 0000 UTC for the CONT simulation. Cross section taken at same latitude as P-3 transect, averaged over 6 points in the north-south direction. Longest vectors are approximately 20 m s^{-1}.

and formed the vertical circulation needed to facilitate compensating divergence aloft in the stable layers. This vertical circulation led to a rapid intensification of the moisture gradient in the late afternoon hours. Ziegler et al. (1995) noted that the sloping terrain was not necessary for the formation of the vertical circulation due to the dominant influence of the horizontal thermal gradient via the solenoidal term in the y-vorticity equation. However, they speculated that a combination of sloping terrain and a thermal gradient with increasing temperatures up the slope would produce the strongest circulations.

Since all of the simulations were initialized with the same atmospheric conditions, a horizontal virtual potential temperature gradient appears in each of them initially along the sloping terrain. Because the soil moisture and vegetation modulates the sensible heat flux, a change in these parameters should affect the intensity

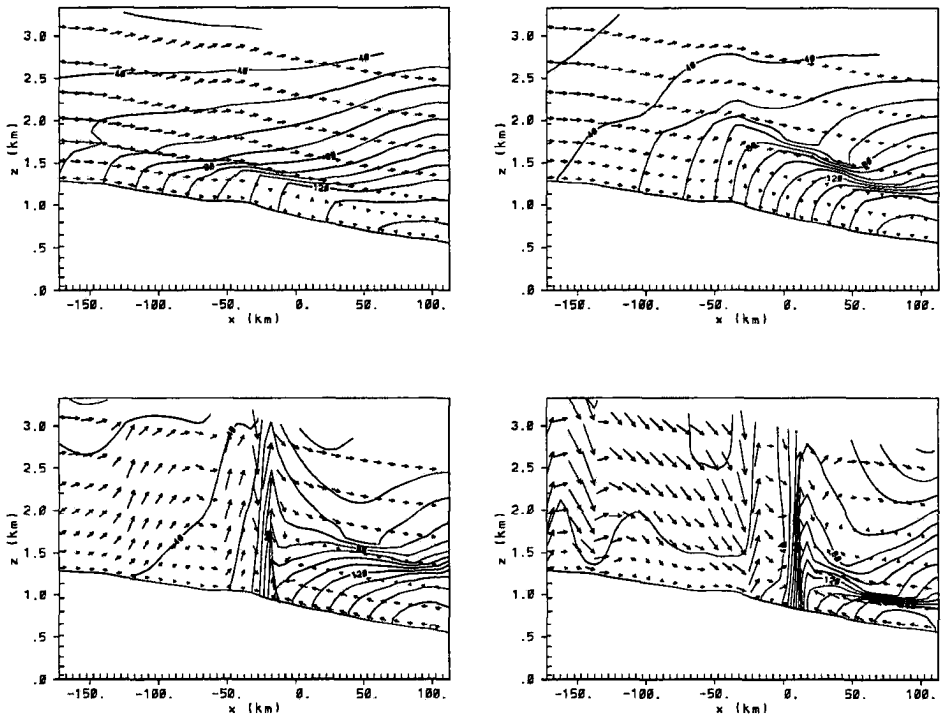

Figure 4.3: Same as 4.2, but for mixing ratio (dg kg^{-1}).

of the thermal and moisture gradients formed. Decreasing the soil moisture east of the dryline would provide less latent heating and more sensible heating to the atmosphere, allowing it to heat slightly more rapidly than in the CONT run. All else being equal, this should act to decrease the afternoon gradient of virtual potential temperature. Looking at the same cross section, Figure 4.4 shows that this is exactly what occurred. While the western portion of the grid showed no difference, the eastern portion had higher virtual potential temperatures by 1800 UTC in both the 50SM and HOMD run. The reduced solenoidal forcing worked to reduce the surface convergence and resulting moisture gradient. Due to increased sensible heat flux, the eastern CBL grew deeper in these two cases (note negative difference contours in Figure 4.4).

The effect of vegetation is not as straightforward. By increasing LAI in the model flux calculations in the MLAI run, both the sensible and latent heat fluxes

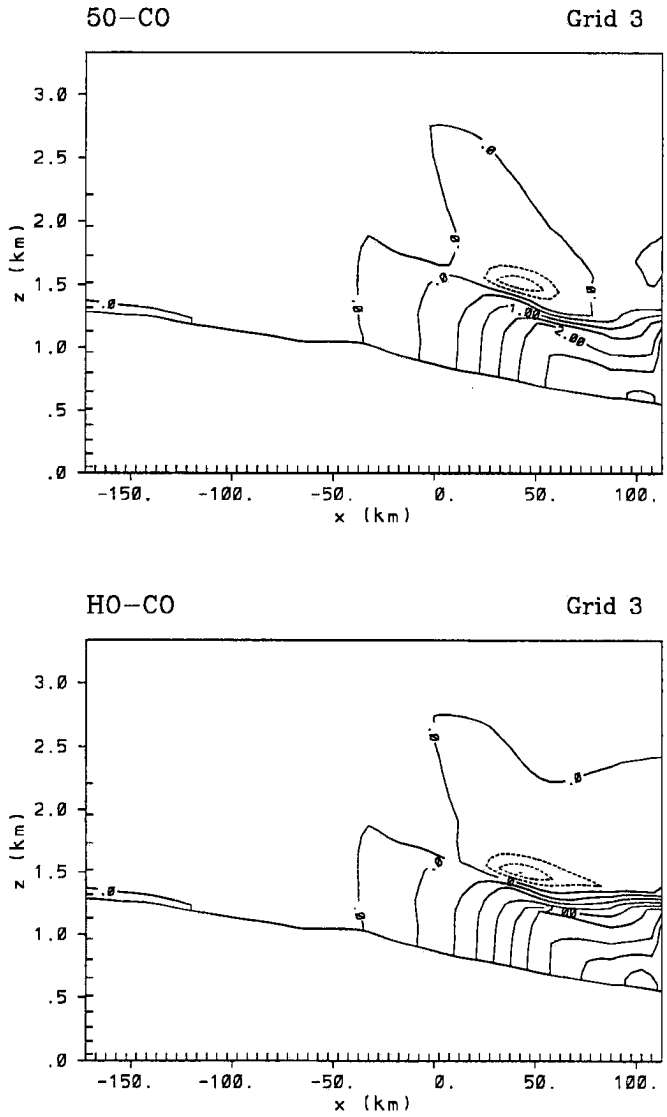

Figure 4.4: 50SM minus CONT (top) and HOMD minus CONT (bottom) virtual potential temperature difference (K) at 1800 UTC for same cross section as 4.1. Contour interval of 0.5 K.

were increased. The expected result is that the model would be slightly warmer and moister in the lower levels. Because of the non-linear interaction between the sensible and latent heat fluxes, it is not clear exactly on which one the LAI would have a dominant effect. The plot of virtual potential temperature difference at 1800 UTC in Figure 4.5 shows that the values were higher near the surface for the MLAI run. Other results seem to indicate that the predominant effect of increasing the LAI is an increased moistening of the lower levels. This is probably because plants can extract water from deep in the soil which could not otherwise be directly transferred to the atmosphere. Differences between the CVEG and CONT runs were imperceptible in the cross section plots. It will be shown that the primary effect of using a constant vegetation type is a smoothing of the results.

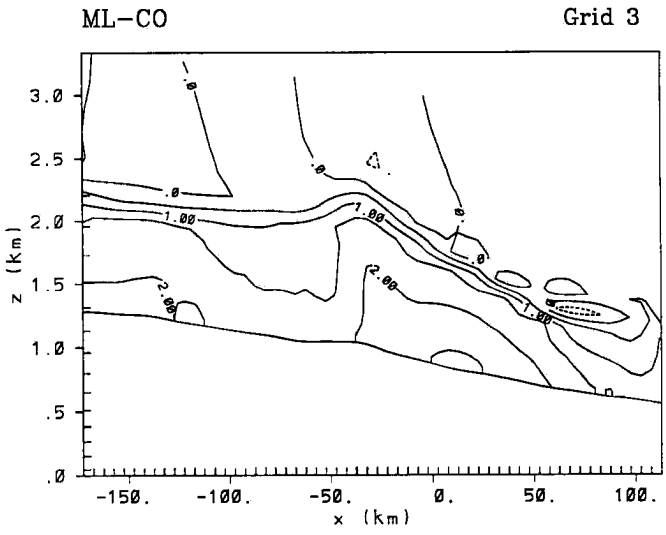

Figure 4.5: Same as 4.4 for MLAI minus CONT.

The raw data from the lowest model grid level over these cross sections was used to generate horizontal profiles of the modeled surface conditions across the dryline at 0000 UTC. Based on the surface mixing ratios depicted in Figure 4.6, the CONT, MLAI, and CVEG simulations were very similar. The moisture gradient across the dryline was a little sharper than the CONT run in the CVEG and LAI

simulations and was slightly farther west. The most obvious differences were in the 50SM and HOMD simulations. The moisture gradient in each of these simulations was much weaker than the CONT simulation and was farther east. Additionally, the environment east of the dryline was much drier. Apparently, the additional moisture flux provided by the vegetation from the deeper soil layers may be important in providing a sustaining moisture source east of the dryline.

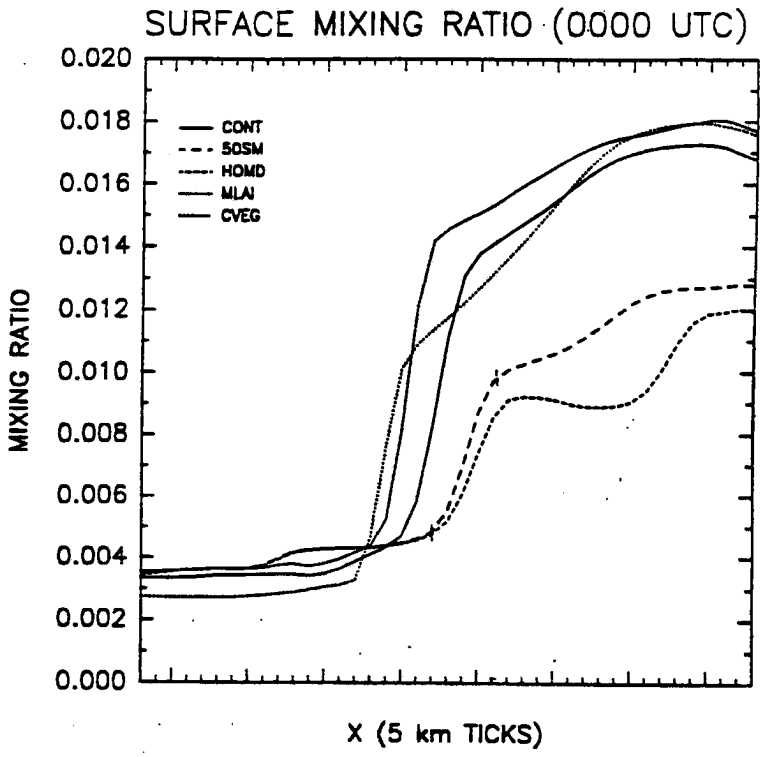

Figure 4.6: West to east horizontal profile of surface mixing ratio at 0000 UTC for each of the simulations for same cross section as 4.1.

Figure 4.7 shows the surface virtual potential temperature profiles. Once again, the CONT, MLAI, and CVEG runs all have similar profiles with slightly different magnitudes. As mentioned previously, the MLAI run tended to be slightly moister and warmer but captured the overall pattern. The virtual potential temperature has a maximum value coinciding with the region immediately west of the dryline in all of the simulations. In the CONT, MLAI, and CVEG runs, the values decrease steadily to the east. The 50SM and HOMD runs also show decreases to the east of the noted

moisture steps, suggesting a bifurcation of the solenoidal forcing. Considering the entire boundary layer east of the westernmost boundary in the 50SM and HOMD runs, the average profile does not exhibit as large a decrease to the east as in CONT, MLAI, and CVEG. The double-step profile in the 50SM and HOMD cases correspond to the multiple dryline structure mentioned earlier.

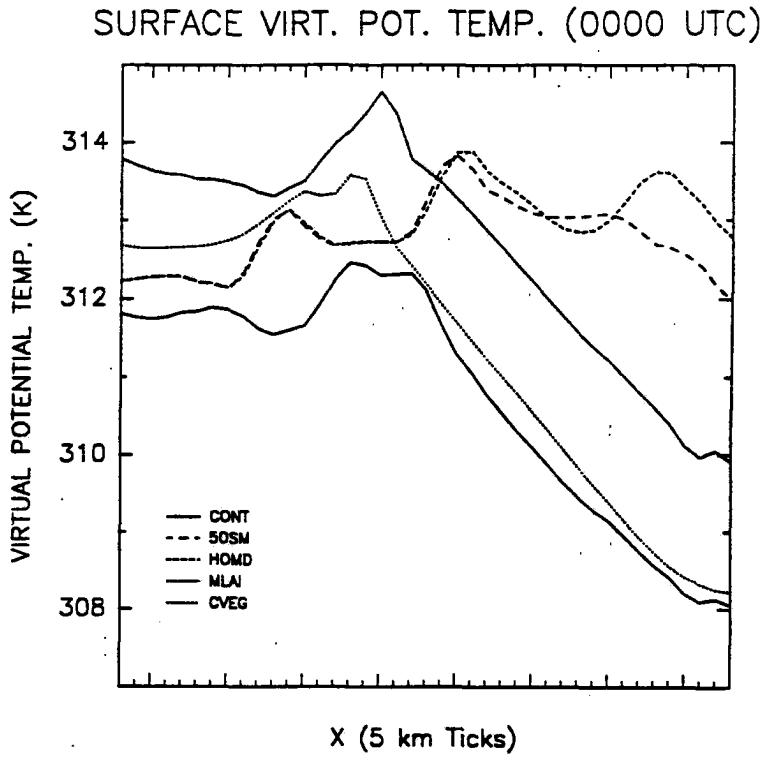

Figure 4.7: Same as 4.6 for virtual potential temperature (K).

Following the same methodology as Ziegler et al. (1995), comparisons have been made between the virtual potential temperature gradient, perturbation pressure gradient, and maximum divergence throughout the day. Time series plots of these field from the area of the dryline are shown in Figure 4.8 for the CONT and HOMD simulations. The values for the virtual potential temperature gradient were calculated based on the profile from the maximum value located near the dryline to 100 km east of this point. The perturbation pressure gradient was calculated the same way but from the point of minimum perturbation pressure at the dryline.

The value for maximum convergence was taken as the maximum value of surface convergence located at the dryline. The plots for CVEG and MLAI (not shown) were very similar in pattern to the CONT simulation, with individual values having higher magnitudes. The 50SM results were very similar to the HOMD results.

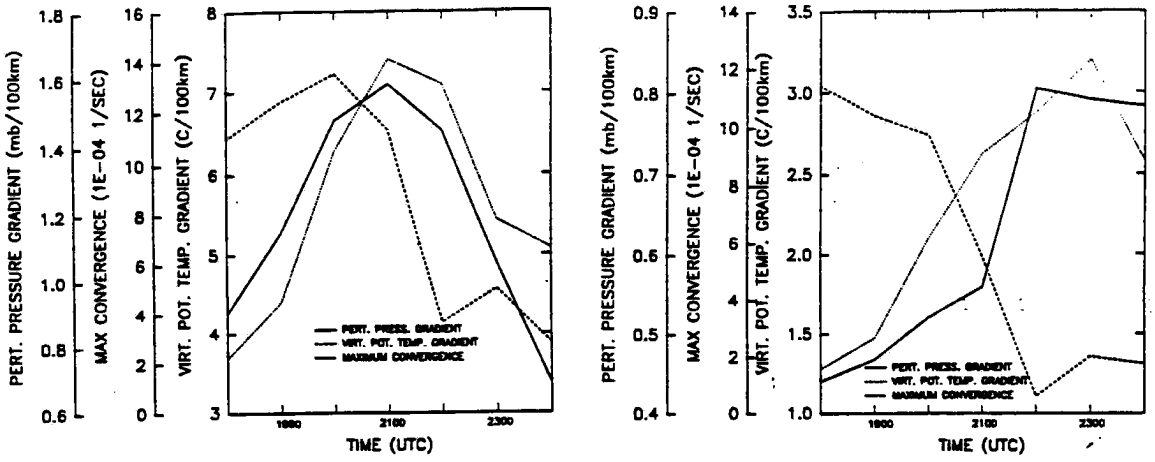

Figure 4.8: Time series of perturbation pressure gradient (mb (100 km)$^{-1}$), virtual potential temperature gradient (K (100 km)$^{-1}$), and maximum convergence at the dryline (10^{-4} sec^{-1}) for the CONT run (left) and HOMD run (right). Values calculated from the same cross section as 4.1.

The most interesting feature seen in all of these plots is that the maximum convergence and pressure gradient occurs after the maximum gradient of virtual potential temperature. In the CONT, CVEG, and MLAI runs the difference is only about an hour. However, in the HOMD and 50SM simulations it is a few hours. This is in direct contrast with the results of Ziegler et al. (1995), which showed maximum thermal and moisture gradients occurring after the time of maximum convergence. It is not clear why the results should be different. Possible explanations may lie in the fact that their simulations were two-dimensional, making it very difficult to

compare their results with ours. Additionally, the data shown here represents only one small slab of the model's three-dimensional results. There may be other cross sections which exhibit behavior similar to that seen in Ziegler et al. (1995). There do appear to be some segments of the dryline on the horizontal plots which have increasing thermal and moisture gradients throughout the day. If this is indeed the case, there may be different mechanisms working to form the dryline at different locations along its length. In any event, the presence of kinematic frontogenetic forcing at the dryline is supported by these simulations.

4.1.2 Horizontal Analysis

Because only the southern portion of the dryline was in the immediate vicinity of a soil moisture gradient in the CONT simulation, it is necessary to examine how the entire dryline evolved differently between each of the simulations. A very narrow area of strong moisture convergence first became well defined in the simulations at 2000 UTC, so comparisons will first be made at this time to see differences in dryline formation.

The vertical cross-section analysis indicated that the strength of the horizontal virtual potential temperature gradient and degree of stratification was critical in the evolution and strength of the dryline. Figure 4.9 shows the surface analysis of the virtual potential temperature from the CONT simulation at 2000 UTC. A strong east to west gradient was located over the eastern Texas Panhandle at this time. The gradient was most pronounced in the area of moist soil, near the extreme southwest corner of Oklahoma. A zone of maximum virtual potential temperature was analyzed from southwest Kansas through the central Oklahoma and Texas Panhandles. This area was just west of the dryline location.

Figure 4.10 shows the model results for the same field for the rest of the simulations. Each of the simulations exhibited a virtual potential temperature gradient in the eastern Panhandle. The gradient in the 50SM was considerably weaker, and

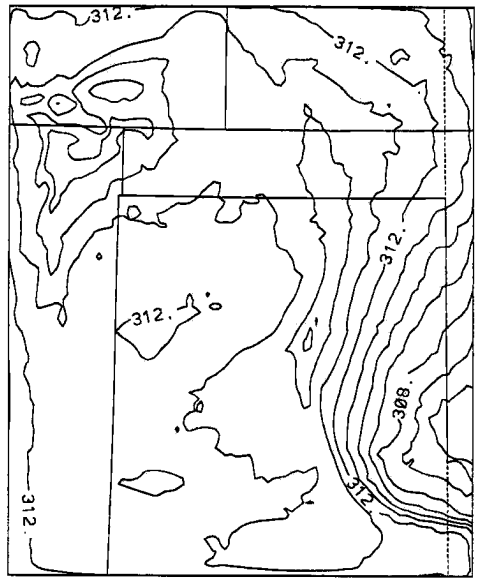

Figure 4.9: Surface virtual potential temperature analysis (K) at 2000 UTC from the CONT simulation. Contour interval of 1 K.

the HOMD gradient was weaker yet. The largest deviation in these two simulations was in the area of the CONT simulation's moist soil patch, but the strength of the gradient was also somewhat affected in all portions of the dryline. The maximum gradient of virtual potential temperature occurs slightly farther east in the CONT simulation, closer to the moist soil patch. In the 50SM and HOMD runs, the maximum gradient location seems to be forced more by the sloping terrain. Although the northern sections of the dryline are not in the immediate vicinity of the soil moisture gradient in the CONT simulation, there was moist soil farther to the east and south on grid 2 which could have contributed to the moisture content of air advected into grid 3 later in the day.

Although the MLAI simulation is very comparable to the CONT simulation as far as the strength of the virtual potential temperature gradient, careful examination reveals that the values of the contours are about 2 to 4 degrees K higher across the domain. This is due to the increased warming and moistening provided by the increased LAI. Because contrasts in LAI across varying vegetation types are also stronger in this run, the model results appear to be "noisier". In contrast, the

Figure 4.10: Same as 4.9 for the 50SM (top-left), HOMD (top-right), MLAI (bottom-left), and CVEG (bottom-right) simulations.

CVEG simulation results are very smooth. Both the strength of the gradient and the contour values are comparable to the CONT simulation.

Since the virtual potential temperature gradient directly influences the strength of the horizontal hydrostatic pressure gradient, this field has also been examined. Figure 4.11 shows the perturbation pressure for the CONT simulation at 2000 UTC calculated from the model output perturbation Exner function. This is the pressure gradient to which the model's winds respond, so it is appropriate to use this variable as an estimate of the pressure gradient strength. A trough of perturbation pressure extends from southwest Kansas across the central Oklahoma and Texas Panhandles corresponding to the virtual potential temperature maximum. This trough enhances the upslope flow to the east, thereby aiding convergence along the dryline.

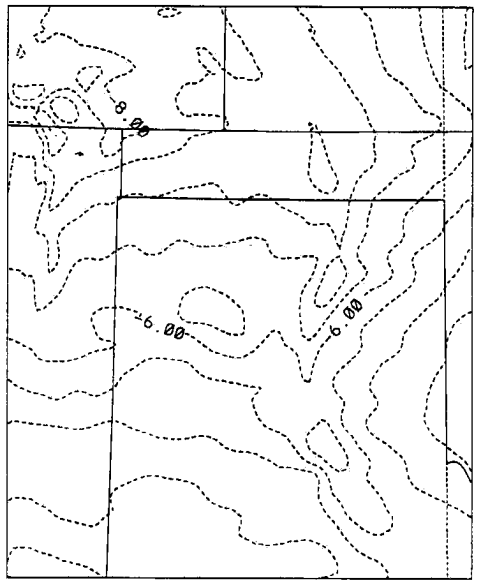

Figure 4.11: Same as 4.9, but for perturbation pressure (mb, contour interval 0.5 mb.)

Figure 4.12 shows the same field as Figure 4.11 for each of the sensitivity test runs. The same trough was produced in all of the simulations in varying degrees, with the MLAI run producing the deepest trough and strongest pressure gradient to the east. The 50SM and HOMD simulations produced a weaker pressure gradient

than the CONT run, so it is expected that the surface convergence at the dryline was also reduced. In all of the simulations, a mesoscale low pressure develops in the northern Texas Panhandle. This may be a result of the southeasterly winds coming over the south rim of the Canadian River Valley, thus inducing a lee-side trough effect. The low center is slightly farther west in the HOMD and 50SM runs, possibly due to the fact that the maximum gradient in virtual potential temperature is slightly farther west, as mentioned previously.

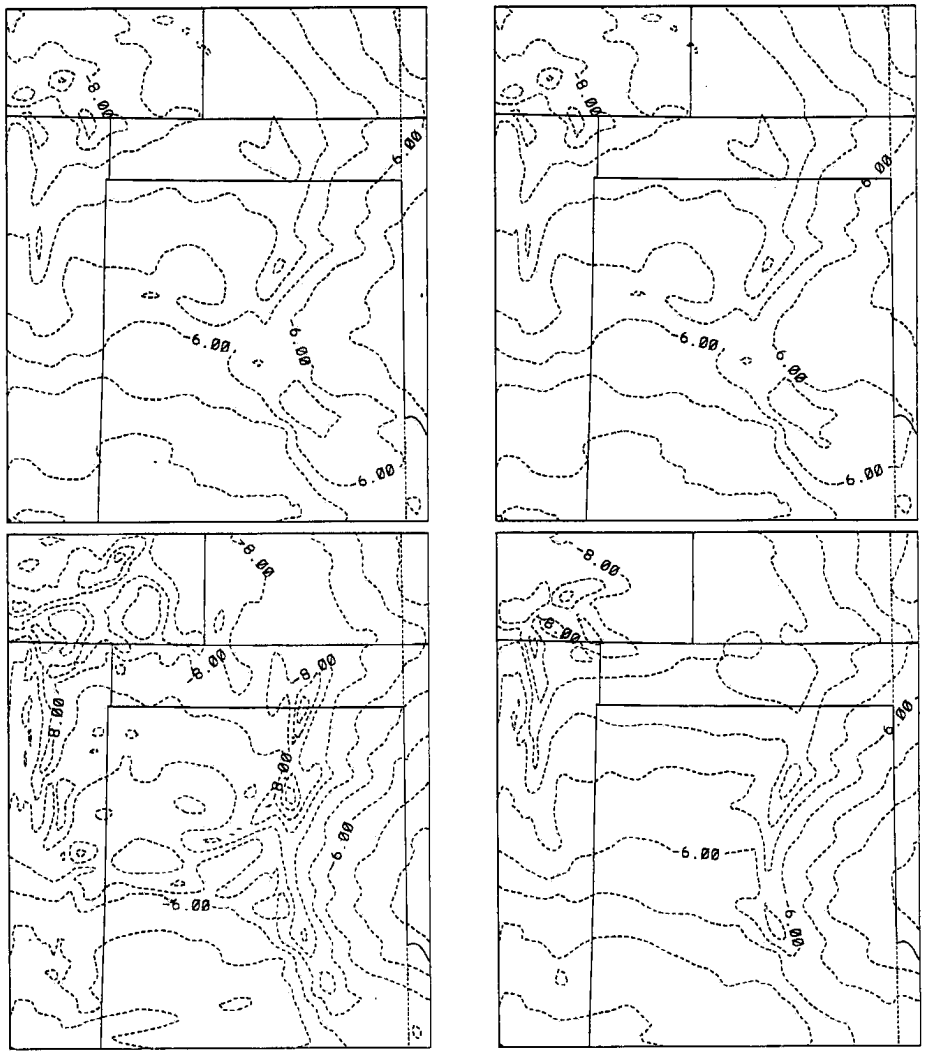

Figure 4.12: Same as 4.10, but for the 50SM (top-left), HOMD (top-right), MLAI (bottom-left), and CVEG (bottom-right) simulations.

Positive vertical velocities at 1.5 km AGL exceeding 0.1 m s^{-1} are plotted in Figure 4.13 for the CONT run at 2000 UTC. This plot gives a good indication of the convergent zone corresponding to the dryline. The dryline at this time exhibits a backwards "s" shape. The maximum upward motion of almost 2 m s^{-1} occurs near the inflection point of this wavelike feature and is clearly related to the mesoscale low pressure feature in Figure 4.11. The same field is shown for the other simulations in Figure 4.14. The shape of the dryline is similar in all of the simulations with the exception of the MLAI run where the dryline is straighter. The maximum vertical velocity in the 50SM and HOMD simulations is on the order of 1 m s^{-1}, half that of the CONT run. Vertical velocities in the MLAI and CVEG simulations are much higher, approaching 5 m s^{-1}. The vertical motion bands west of the dryline are better developed in MLAI than in other runs, suggesting a connection between these boundary layer structures and increasing sensible heat flux.

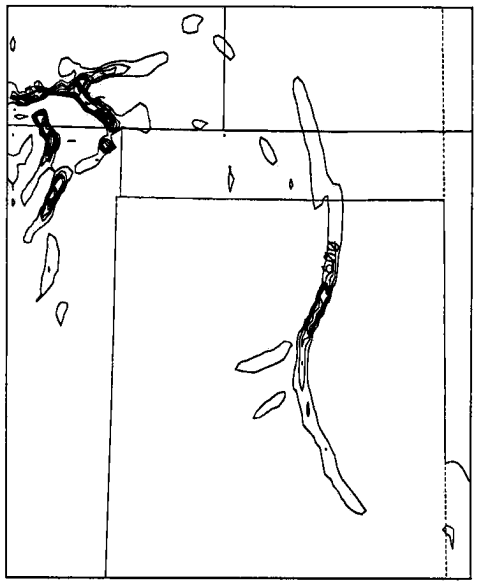

Figure 4.13: Same as 4.9, but for upward vertical velocities greater than 0.1 m s^{-1} at approximately 1500 m AGL. Contour interval of 0.5 m s^{-1}.

One of the most interesting differences is very subtle to the naked eye but is visible if the plots are overlayed on a light table. The data from the cross sections

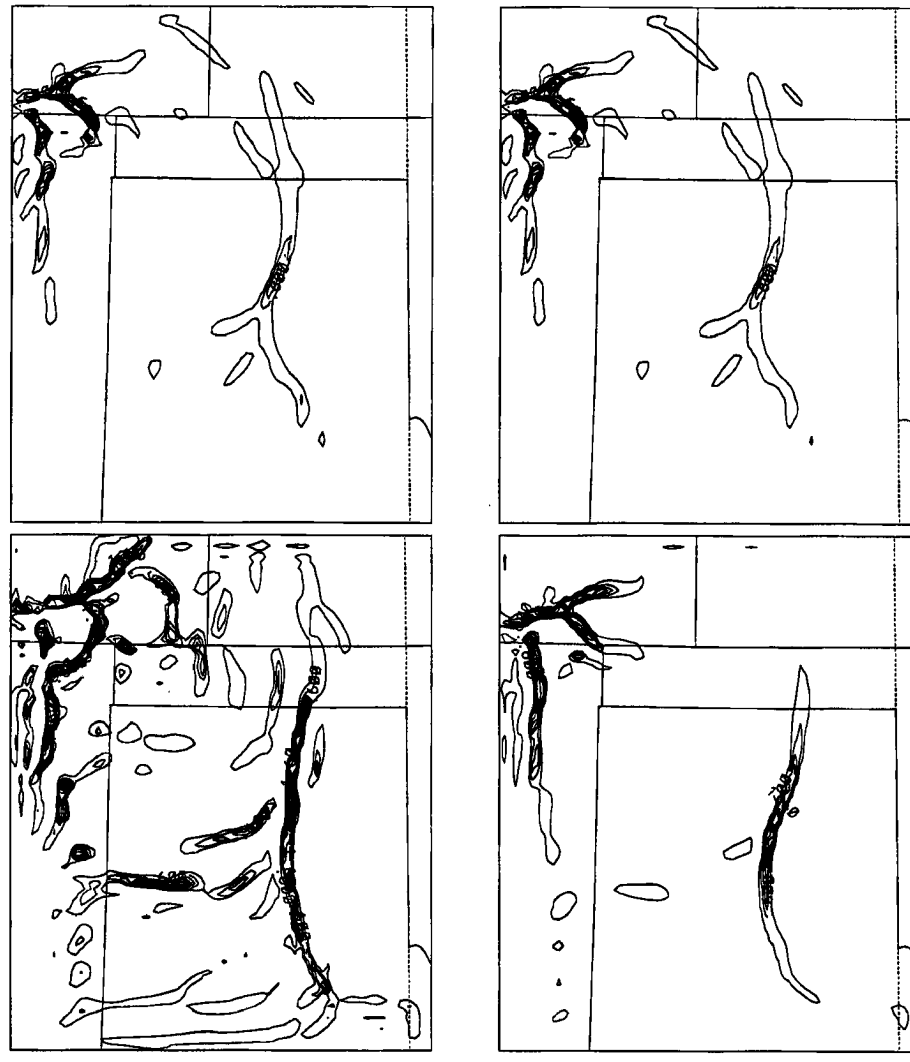

Figure 4.14: Same as 4.10, but for the 50SM (top-left), HOMD (top-right), MLAI (bottom-left), and CVEG (bottom-right) simulations.

shown earlier indicated that the dryline moved farther east in the 50SM and HOMD simulations than in the CONT run. Recall that this data was averaged over 6 grid points at each longitude and cross section was taken near the middle of the dryline just south of where the infection point is located. If the position of the dryline is assumed to correspond identically with the vertical motion field, then the northern two-thirds of the dryline in the 50SM and HOMD simulations actually formed slightly farther west than in the CONT run. The dryline in these two simulations then continued to progress eastward more rapidly than in the CONT run, thus travelling farther east by the end of the simulation. This faster movement east supports the findings of Ziegler et al. (1995). They speculated that the net dryline motion is a result of the balance between the westward density current-like movement and the eastward movement due to advection by the prevailing westerlies west of the dryline. Since the virtual potential temperature gradient is weaker in the dry soil cases, the density current component is weaker, thus allowing the advection component to have more of an impact.

During the following hours, the dryline formed rapidly along the zone of convergence. Figure 4.15 shows the lowest model level mixing ratio and winds at 2300 UTC from the CONT simulation. The dryline is visible as a continuous band of strong moisture gradients extending from southwest Kansas through the east-central Texas Panhandle, with an eastward bend near Childress, Texas. Although the grid is too coarse to explicitly resolve convection, the model did generate "pseudo-convective" clouds and warm rain in southwestern Kansas and the Oklahoma Panhandle, and this is evident as divergent mesocale outflows in the surface fields. The most intense moisture gradient occurs at the eastward bend in the dryline near Childress where the soil moisture contours parallel the topographic contours. The high soil moisture area created a local minimum of virtual temperature, and a resulting mesoscale circulation formed, enhancing the easterly component of the winds and forcing convergence against the northwest to southeast oriented ridge in the topography.

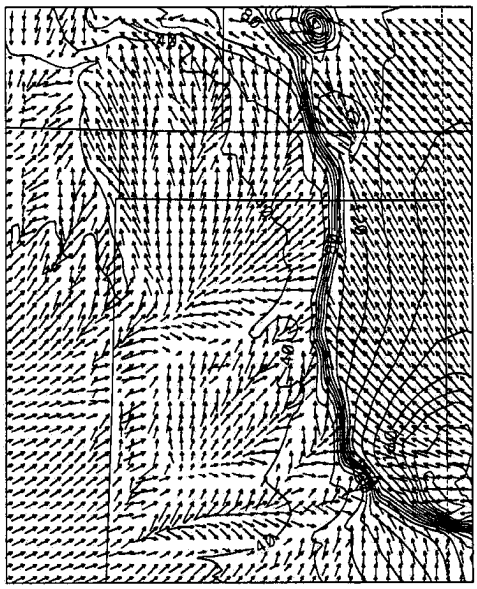

Figure 4.15: Total mixing ratio (dg kg^{-1}) and winds from the CONT simulation at 2300 UTC. Longest vectors represent approximately 15 m s^{-1}.

Figure 4.16 shows the 2300 UTC mixing ratio and winds for the other simulations. The moisture gradient in the 50SM and HOMD runs is much weaker, and is not continuous through the Texas Panhandle. The gradient in these runs becomes diffuse southeast of Amarillo. Note that the winds have much less of an easterly component in the Childress area than in the CONT simulation in these runs. This prevented strong moisture convergence from occurring against the ridge to the southwest as occurred in the CONT run. Additionally, the atmosphere east of the dryline is much drier. In contrast, the results from the MLAI simulation show an intense continuous dryline similar to the CONT simulation, but the atmosphere to the east has a much higher moisture content than the CONT run. The CVEG run is most similar to the CONT run, but the moisture maximum northeast of Childress is much larger and more uniform. The location and intensity of "pseudo-convection" produced by the model also varies between simulations.

Color computer time-lapse animation of the horizontal moisture flux divergence proved to be the best way to quickly see the formation and morphology of the dryline from the model data. Although the dramatic effect of animation cannot be captured

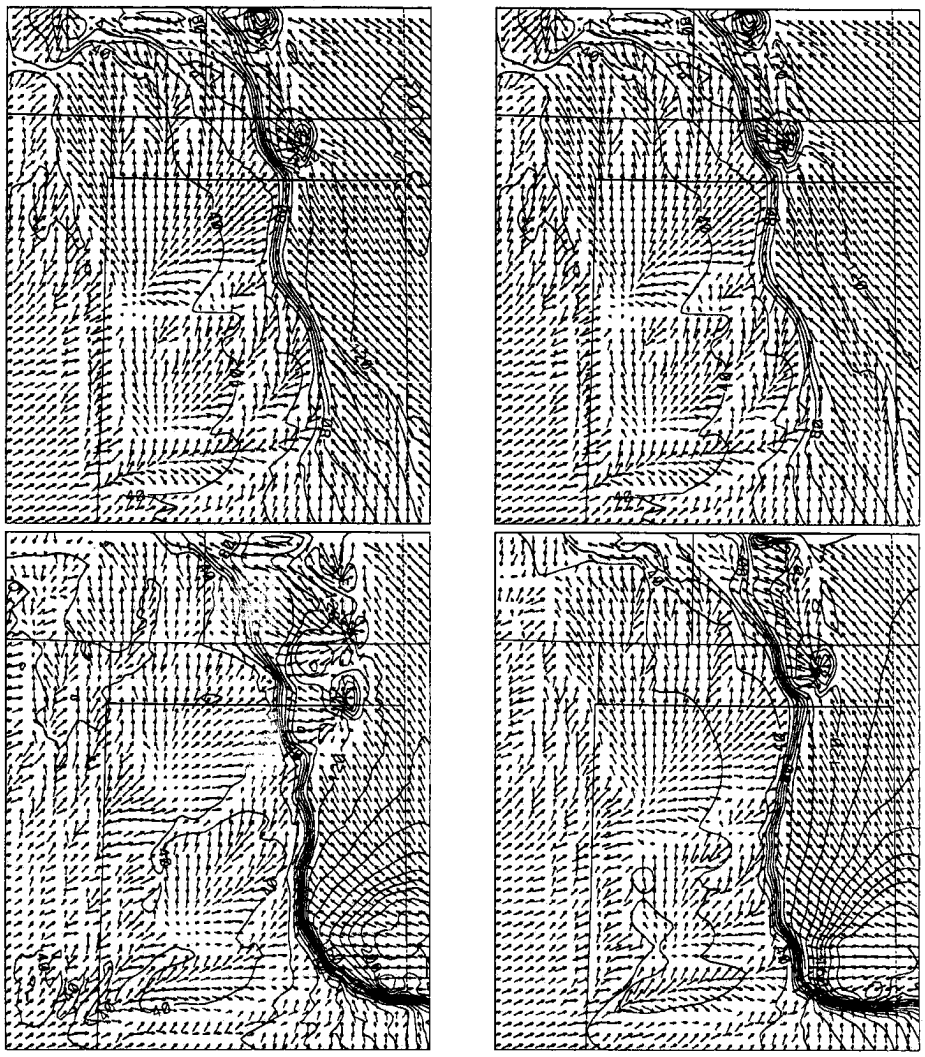

Figure 4.16: Same as 4.15, but for the 50SM run (top-left), HOMD run (top-right), MLAI run (bottom-left), and CVEG run (bottom-right).

in print, the difference in dryline structure between the CONT and HOMD simulations is evident in Figure 4.17. This figure shows the horizontal moisture flux divergence at 0000 UTC for these two simulations. The dryline is very pronounced in both panels as a very narrow band of strong moisture convergence. As revealed in the plots of mixing ratio, the dryline is one continuous band in the CONT simulation. However, the HOMD run produced a secondary convergence zone east of and parallel to the primary zone. Both bands are oriented parallel to the low-level wind flow and resemble typical convective rolls. The southwest to northeast bands of convergence present west of the dryline in both simulations are not fully understood but may be a result of horizontal convective roll circulations typical of a highly sheared, convectively unstable environment. It is intriguing that these roll-like features appear to produce small-scale undulations on the dryline at intersection locations, suggesting a connection to studies of "dryline wave" generation by McGinley and Sasaki (1975) and Koch and McCarthy (1982) and a sea-breeze study by Wakimoto and Atkins (1994).

Another interesting feature in these two figures is the indication of a convective cell generated by the model in the north-central Oklahoma Panhandle. This is the cell from which the model produced significant rainfall. An outflow boundary can be seen propagating outward towards the south and interacting with the dryline as the cell moves northeast. While this is most apparent in the HOMD simulaton when animated (see Appendix), it is present in all simulations. In Figure 4.17, the storm is apparent as a strong convergence/divergence couplet. Plots of the non-hydrostatic pressure and vertical motion (not shown) reveal that the model actually resolved the classic storm updraft and rear flanking downdraft structure. This simulated convective cell is the focus of an ongoing study.

Similar figures from 1900 UTC through 0000 UTC for all simulations are included in the Appendix. It appears from the animation of these fields that the

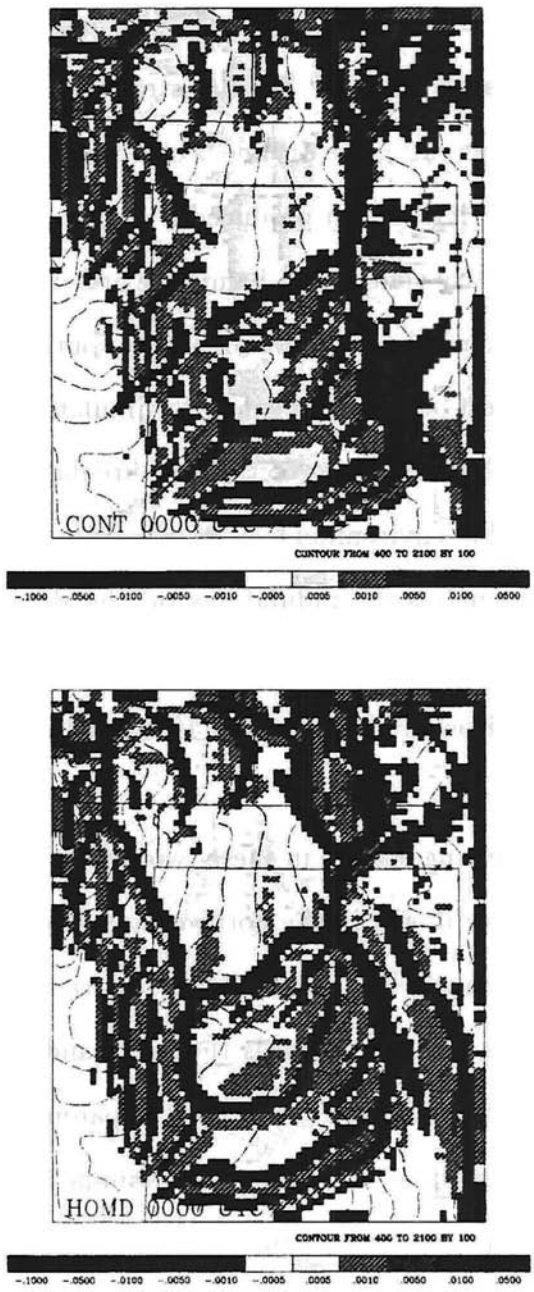

Figure 4.17: Horizontal moisture flux divergence (g kg^{-1} s^{-1}) at 0000 UTC for the CONT run (top) and 50SM run (bottom). Warm colors indicate divergence, with cool colors indicating convergence. Values on scale correspond to the minimum value for each color increment. Topography contours (m) are overlaid.

detailed topography plays a key role in dryline formation and morphology. Preferred areas for moisture convergence are along the ridges and edges of valleys, with strong moisture divergence occurring in the valleys. Further sensitivity tests are required, but it is hypothesized that the heating of the sloping terrain along the ridges generates boundary layer eddies with their axes roughly parallel to the flow. Compensating downdrafts occur between the ridge lines, causing subsequent moisture divergence in the valleys. This could explain the strong moisture divergence observed in the Canadian River valley. This study documents these convective rolls in the dryline environment for the first time.

4.2 Pre-storm Environment

The environment east of the dryline is typically ripe for convection. It was mentioned earlier that drylines often act as the trigger for convection, and that thunderstorms actually developed along the dryline on this day. The model results can be used to determine the impact of the varying surface conditions on the pre-storm environment. Forecasters utilize such output from observations and models to predict the formation of potentially severe weather, so it is useful to see what impact the use of variable soil moisture and vegetation fields may have on convective parameters.

Figure 4.18 shows the CAPE on grid 3 at 2000 UTC from the CONT simulation. The values were calculated based on an average of the lowest 1 km of data. A strong gradient of CAPE exists along the dryline. CAPE reaches a maximum over the moist soil patch and all along the eastern edge of the grid, where low-level atmospheric moisture was abundant. Values ranged from 0 J kg^{-1} west of the dryline to near 3000 J kg^{-1} at the eastern edge of the grid.

Figure 4.19 shows the CAPE for each of the sensitivity simulations at 2000 UTC. The 50SM and HOMD simulations look very similar to the CONT run, with the CAPE being reduced over the eastern portion of the grid. As the soil moisture

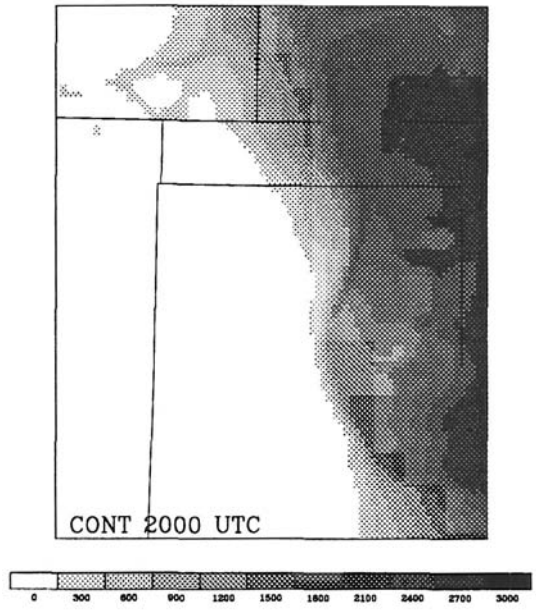

Figure 4.18: CAPE (J kg^{-1}) for the CONT simulation at 2000 UTC. Values on scale represent the minimum value of each color increment.

is reduced, moisture flux from the ground into the atmosphere is reduced, thus reducing the CAPE east of the dryline. Surprisingly, the CAPE seemed to be the most affected in the MLAI and CVEG simulations. While the patterns were similar, the maximum values were higher, especially in the MLAI simulation where much of the domain east of the dryline actually exceeded 3000 J kg^{-1}. A very narrow band of higher CAPE was also evident along the dryline in all runs, but was especially pronounced in the MLAI simulation. This high-CAPE band is a result of intense localized horizontal moisture convergence and deepening of the moist layer at the dryline. The small patches of maximum CAPE that occur in the MLAI simulation could be significant once convection develops in determining which storms would have the highest severe potential.

Another severe weather forecasting parameter is the storm relative environmental helicity (SREH). To compute the SREH from the model output, a storm motion had to be assumed. To make the calculation uniform among all of the simulations, an assumed storm motion was calculated at each grid point. The storm motion was assumed to be 75 percent of and 30 degrees to the right of the mean wind from 3

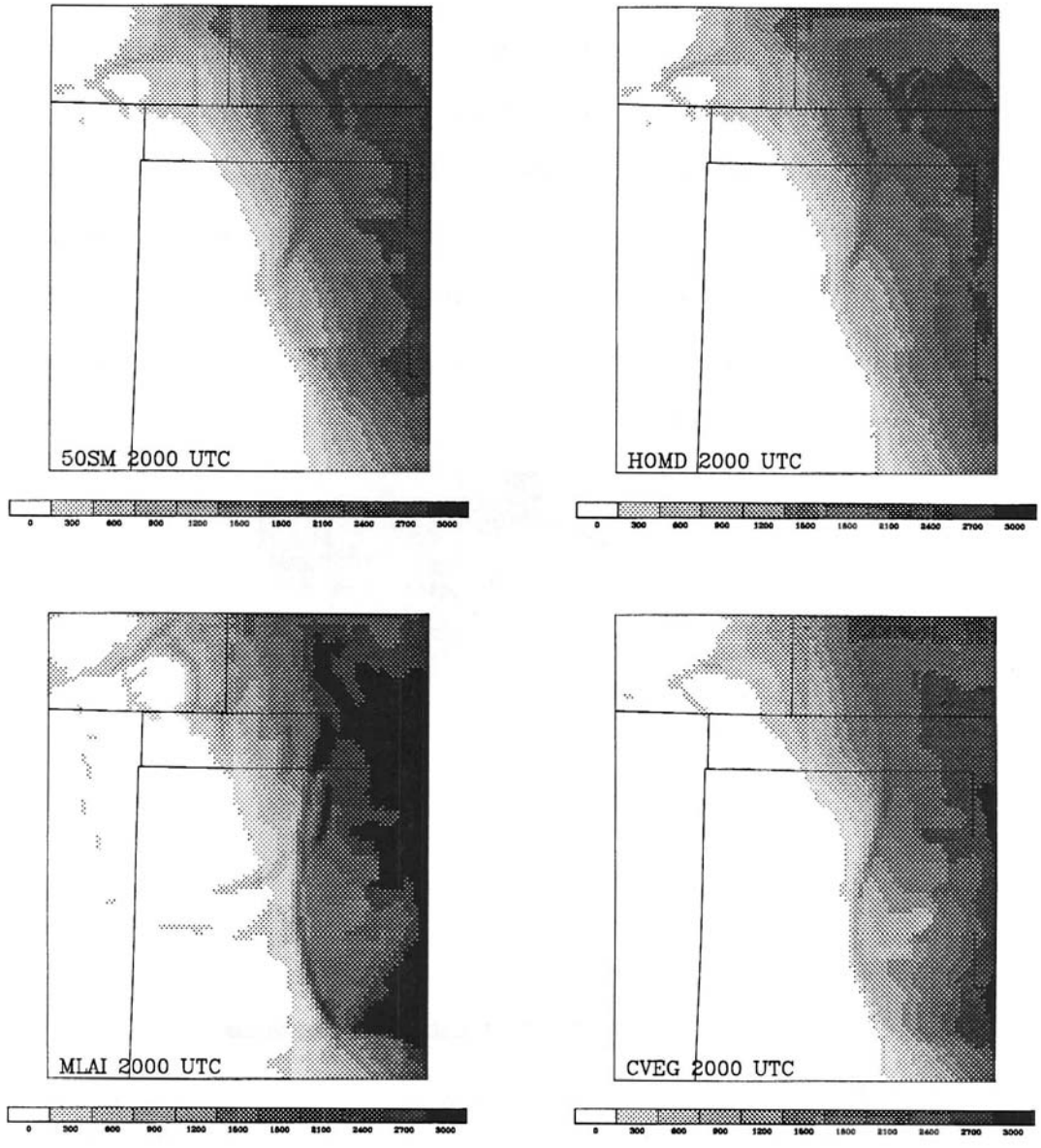

Figure 4.19: Same as 4.18, but for the 50SM run (top-left), HOMD run (top-right), MLAI run (bottom-left), and CVEG run (bottom-right).

km to 10 km. This storm motion was then used to calculate the SREH from 0 to 4 km over the entire grid 3 domain for each of the simulations.

Figure 4.20 shows the SREH at 2000 UTC for the CONT simulation for all points where CAPE exceeded 500 J kg^{-1}. As in the CAPE field, SREH undergoes significant gradients along portions of the dryline. Large areas east of the dryline have SREH values greater than or equal to 100 m^2 s^{-2}, and an area of maximum SREH exceeding 200 m^2 s^{-2} occurs near Childress, Texas. This is a result of the easterly winds induced by the strong virtual potential temperature gradient around the edge of the moist soil patch. Since this affects only the lowest model levels, the winds above the CBL are southwesterly, leading to a strong veering of the wind with height and strong SREH.

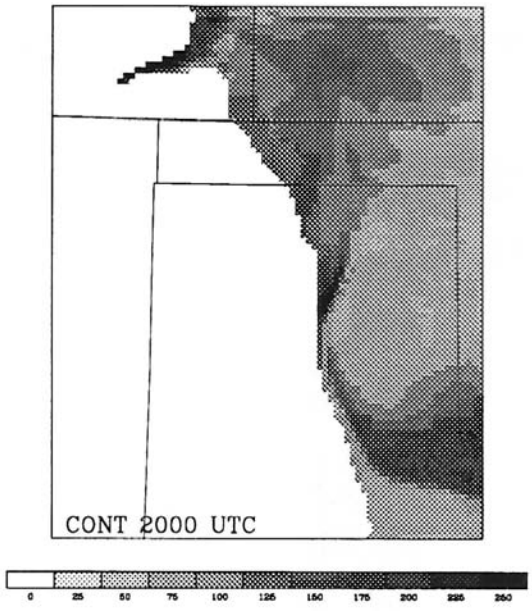

Figure 4.20: Storm-relative environmental helicity (m^2 s^{-2}) at 2000 UTC from the CONT simulation. SREH is only plotted at points where the CAPE equals or exceeds 500 J kg^{-1}. Values on the scale represent the minimum value for each color increment.

Figure 4.21 shows the SREH for the other four simulations at 2000 UTC for all points where CAPE exceeded 500 J kg^{-1}. There is no evidence of a SREH maximum in the Childress area in the 50SM and HOMD simulations. This highlights the

importance of the soil moisture effect on the low-level winds. In the MLAI simulation, the maximum is more pronounced than in the CONT simulation, due to the increased cooling over the moist soil and the stronger virtual potential temperature gradient in this area. All of the simulations produced a maximum in SREH along the southern rim of the Canadian River Valley in varying degrees. The effects of this river valley are not fully understood and require further study as mentioned previously.

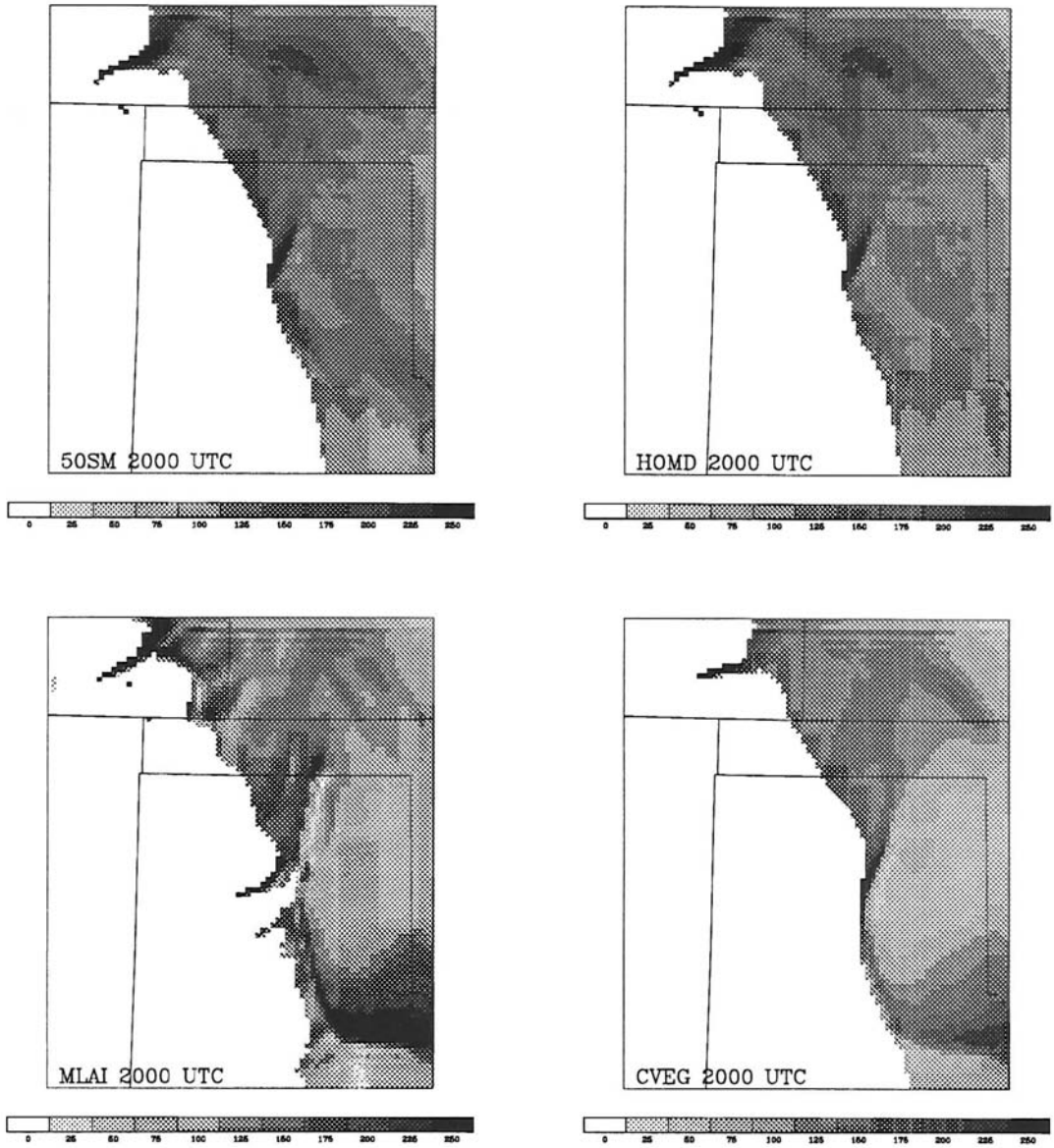

Figure 4.21: Same as 4.20, but for the 50SM run (top-left), HOMD run (top-right), MLAI run (bottom-left), and CVEG run (bottom-right).

Chapter 5

SUMMARY AND CONCLUSIONS

Five simulations of a Great Plains dryline using a three-dimensional mesoscale model have been presented. The CONT simulation employed a realistic API-derived soil moisture field and BATS vegetation dataset with a limit on LAI in the surface flux calculations. This run generated the most realistic solution when compared to the observations. Two other simulations, the 50SM and HOMD runs, were initialized with a reduced soil moisture field and a homogeneous dry soil moisture field, respectively. The remaining simulations used the same soil moisture field as the CONT run, but with perturbations of the vegetation data. The MLAI simulation utilized the variable BATS dataset with no limit applied to the LAI in the surface flux calculations. The CVEG run was initialized with a constant vegetation type of short grass over the entire domain.

The changes of the land surface conditions in each of the sensitivity runs affected the modeled sensible and latent heat fluxes, causing differences in how the dryline and the prestorm environment east of the dryline evolved throughout the afternoon. The 50SM and HOMD simulations appeared to have the greatest effect on the structure and movement of the dryline compared to the CONT simulation. The reduced latent heat flux east of the dryline reduced the east to west gradient of virtual potential temperature, thus reducing the magnitude of the "density current" term as proposed in the theoretical model of dryline motion proposed by Parsons et al. (1991) and Ziegler et al. (1995). This allowed the dryline to move farther east at a more rapid speed than the CONT simulation. One puzzling feature of

these two simulations was the formation of the dryline slightly farther to the west than the CONT simulation in the region of the Canadian River Valley. It is speculated that the fine scale topographic features have an impact on the development of boundary layer eddy circulations, thus affecting preferred formation locations. Further sensitivity tests using varied topographic datasets are required to test this hypothesis.

The MLAI simulation produced results similar to the CONT run but was generally warmer and moister in the CBL both east and west of the dryline. This led to an over-prediction of atmospheric moisture content at the lowest model level, especially east of the dryline. Values of CAPE and SREH were much higher in the prestorm environment in the MLAI run due to the increased warming and moistening. The strength of the thermal gradients across the dryline was increased due to the increased latent heat flux east of the dryline. It is speculated that the specified values of LAI in the standard BATS model may be too high when the percentage of vegetation coverage and the amount of light reaching leaves at the bottom of the canopy are considered.

The CVEG run generally produced smoother results than any of the other simulations. Model output wind vectors often looked noisy in many of the simulations, and small waves appeared in the contours of most of the thermodynamic variables as a result. Based on the CVEG results, heterogeneous vegetation has a strong effect at smaller length scales, providing small areas where strong gradients of sensible and latent heat fluxes exist. The heterogeneity of the fields produced by variable vegetation may be necessary when forecasting small scale features such as convective storms.

Since the soil moisture field appears to have a first order effect on the formation and morphology of the dryline compared to the vegetation, future work should focus in this area. Additional simulations using various perturbations of the soil moisture

should be run. Because precipitation is not normally distributed, there is also some uncertainty of how to produce the best objective analysis of API. Other sensitivity tests using various wavelength response values in the Barnes analysis of API could be used. Additionally, as cumulative precipitation analyses become available from the new WSR-88D radar, it would be useful to incorporate this information into the generation of soil moisture data. If data such as these were combined with a variable soil type dataset, it is expected that a most realistic soil moisture initialization could be produced utilizing an API scheme.

Future work should also be performed in the area of variable vegetation effects. It is apparent that the heterogeneous vegetation field may be very important for forecasting small scale variations in the wind and thermodynamic fields. Detailed vegetation fields consisting of more than 18 categories might prove useful, as well as the inclusion of more than one vegetation type per grid square, as Lee (1992) has done in his LEAF scheme in RAMS. This would require additional information about physical attributes of each vegetation type.

Future sensitivity tests should be run using LEAF. Additionally, since the adjustment of the surface fluxes by a specified LAI from BATS may be too simplistic, different schemes should be explored. One suggestion would be to determine LAI directly from actual NDVI data as in Lee (1992) and Nemani and Running (1989). This LAI value could be used to modify the surface fluxes and determine albedo and roughness length. Vegetation type and coverage would then be used only to determine stomatal resistance, rooting depth, and other similar parameters. Additionally, a Beer-Bougher relationship could be used to estimate the effect of the vegetation on both the incoming and outgoing radiation within the vegetation canopy, although the plant spacing needs to be considered.

As new methods and data are incorporated in specifying the land surface conditions, our understanding of their effects on the atmosphere should increase. This

will have a direct benefit on new operational mesoscale models, thus improving our ability to forecast short term mesoscale weather events.

REFERENCES

Anthes, R.A., 1984: Enhancements of convective precipitation by mesoscale variations in vegetative covering in semiarid regions. *J. Climate Appl. Meteor.*,**2**, 271-279.

Anthes, R.A., Y.H. Kuo, S.G. Benjamin, and Y.-F. Li, 1982: The evolution of the mesoscale environment of severe local storms: Preliminary modeling results. *Mon. Wea. Rev.*, **110**, 1187-1213.

Avissar, R., and R.A. Pielke, 1989: A parameterization of heterogeneous land surfaces for atmospheric numerical models and its impact on regional meteorology. *Mon. Wea. Rev.*, **117**, 2113-2136.

Bonan, G.B., D. Pollard, and S.L. Thompson, 1993: Influence of subgrid-scale heterogeneity in leaf area index, stomatal resistance, and soil moisture on grid-scale land-atmospheric interactions. *J. Climate*, **6**, 1882-1897.

Brock, F., G. Saum, and S. Semmer, 1986: Portable Automated Mesonet II. *J. Atmos. Ocean. Tech.*, **3**, 373-582.

Beebe, R.G., 1958: An instability line development as observed by the tornado research airplane. *J. Meteor.*, **15**, 278-282.

Benjamin, S.G., 1986: Some effects of surface heating and topography on the regional severe storm environment. *Mon. Wea. Rev.*, **114**, 307-343.

Benjamin, S.G., and T.N. Carlson, 1986: Some effects of surface heating and topography on the regional severe storm environment. Part I: 3-D simulations. *Mon. Wea. Rev.*, **114**, 330-343.

Betts, A.K., 1982: Saturation point analysis of moist convective overturning. *J. Atmos. Sci.*, **39**, 1484-1505.

Betts, A.K., 1984: Boundary layer thermodynamics of a High Plains severe storm. *Mon. Wea. Rev.*, **112**, 2199-2211.

Bluestein, H.B., and S.S. Parker, 1993: Modes of isolated, severe convective storm formation along the dryline. *Mon. Wea. Rev.*, **121**, 1352-1374.

Carlson, T.N., and F.H. Ludlam, 1968: Conditions for the formation of severe local storms. *Tellus*, **20**, 203-226.

Chang, J.-T., and P.J. Wetzel, 1991: Effects of spatial variations of soil moisture and vegetation on the evolution of a prestorm environment: A case study. *Mon. Wea. Rev.*, **119**, 1368-1390.

Clark, C.A., and R.W. Arritt, 1995: Numerical simulations of the effect of soil moisture and vegetation cover on the development of deep convection. *J. Appl. Meteor.*, [in press].

Cotton, W.R., G. Thompson, and P.W. Mielke, Jr., 1994: Real-time mesoscale prediction on workstations. *Bull. Amer. Meteor. Soc.*, **75**, 349-362.

Cram, J.M., and R.A. Pielke, 1987: The importance of synoptic forcing and mesoscale terrain to a numerical simulation of an orographically-induced system. *Proceedings of the 3rd AMS Conference on Mesoscale Processes*, August 21-26, 1987. VAncouver, B.C., Canada, 118-119.

Cram, J.M., R.A. Pielke, and W.R. Cotton, 1992: Numerical simulation and analysis of a pre-frontal squall line. Part I: Observations and basic simulation results. *J. Atmos. Sci.*, **49**, 189-208.

Dickinson, R.E., A. Henderson-Sellers, P.J. Kennedy, and M.F. Wilson, 1986: Biosphere-atmosphere transfer scheme for the NCAR community climate model. Technical Report NCAR/TN-275+STR, NCAR, Boulder, 69 pp.

Dodd, A.V., 1965: Dew point distribution in the contiguous United States. *Mon. Wea. Rev.*, **93**, 113-122.

Estoque, M.A., 1962: The sea-breeze as a function of the prevailing synoptic situation. *J. Atmos. Sci.*, **19**, 244-250.

Fujita, T.T., 1958: Structure and movement of a dry front. *Bull. Amer. Meteor. Sci.*, **39**, 574-582.

Garrett, A.J., 1982: A parameter study of interactions between convective clouds, the boundary layer, and a forest surface. *Mon. Wea. Rev.*, **110**, 1041-1058.

Hane, C.E., C.L. Ziegler, and H.B. Bluestein, 1993: Investigation of the dryline and convective storms initiated along the dryline: Field experiments during COPS-91. *Bull. Amer. Meteor. Soc.*, **74**, 2133-2145.

Keyser, D., and R.A. Anthes, 1977: The applicability of a mixed-layer model of the planetary boundary layer to real-data forecasting. *Mon. Wea. Rev.*, **105**, 1351-1371.

Koch, S.E., and J. McCarthy, 1982: The evolution of an Oklahoma dryline. Part II: boundary-layer forcing of mesoconvective systems. *J. Atmos. Sci.*, **39**, 237-257.

Kosta, R.D., and M.J. Suarez, 1992: A comparative analysis of two land surface heterogeneity representations. *J. Climate*, **5**, 1379-1390.

Lakhtakia, M.N., and T.T. Warner, 1987: A real-data numerical study of the development of precipitation along the edge of an elevated mixed layer. *Mon. Wea. Rev.*, **115**, 156-168.

Lilly, D.K., and T. Gal-Chen, 1990: Can mixing generate buoyancy at the dryline? *J. Atmos. Sci.*, **47**, 1170-1171.

Lanicci, J.M., T.N. Carlson, and T.T. Warner, 1987: Sensitivity of the Great Plains severe-storm environment to soil-moisture distribution. *Mon. Wea. Rev.*, **115**, 2660-2673.

Lee, T.J., 1992: The impact of vegetation on the atmospheric boundary layer and convective storms. Colorado State University Dept. of Atmospheric Sciences Paper, 509, 137 pp.

Lemeur, R., and N.J. Rosenberg, 1979: Simulating the quality and quantity of short wave radiation within and above canopies. Comparison of Forest Water and Energy Exchange Models, ed. by S. Halldin, International Society for Ecological Modelling, Copenhagen, 77-100.

Li, B., and R. Avissar, 1994: The impact of spatial variability of land-surface heat fluxes. *J. Climate*, **7**, 527-537.

Loveland, T.R., J.W. Merchant, D.O. Ohlen, and J.F. Brown, 1991: Development of a land-cover characteristics database for the conterminous U.S. *Photo. Eng. and Rem. Sens.*, **(57)11**, 1453-1463.

Lyons, W.A., D.A. Moon, C.S. Keen, J.A. Schuh, R.A. Pielke, W.R. Cotton, and R.W. Arritt, 1988: Providing operational guidance for the development of sea breeze thunderstorms at the Kennedy Space Center: An experiment using a mesoscale numerical model. *Proceedings of the 15th Conference on Severe Local Storms*, February 1988, Amer. Meteor. Soc., Baltimore, Maryland.

Mahrt, L., 1991: Boundary layer moisture regimes. *Quart. J. Roy. Meteor. Soc.*, **117**, 151-176.

Matteson, G.T., 1969: The west Texas dry freon of June, 1967. M.S. thesis, University of Oklahoma, Norman, 63 pp.

McCarthy, J., and S. E. Koch, 1982: The evolution of an Oklahoma dryline. Part I: A meso- subsynoptic-scale analysis. *J. Atmos. Sci.*, **39**, 225-236.

McCumber, M.C., and R.A. Pielke, 1981: Simulation of the effects of surface fluxes of heat and moisture in a mesoscale numerical model. Part I: Soil layer. *J. Geo. Res.*, **86(C10)**, 9929-9938.

McGinley, J.A., and Y.K. Sasaki, 1975: The role of symmetric instabilities in thunderstorm development on drylines. *Preprints, Ninth Conference on Severe Local Storms*, Amer. Meteor. Soc., Boston, Mass., 173-180.

McGuire, E.L., 1962: The vertical structure of three drylines as revealed by aircraft traverses. National Severe Storms Project Report, No. 7, Kansas City, MO., 11 pp.

Nemani, R., and S.W. Running, 1989: Testing a theoretical climate-soil-leaf area hydrologic equilibrium of forests uing satellite data and ecosystem simulation. *Agric. Forest Meteorol.*, **44**, 245-260.

NNSP (National Severe Storms Project) Staff Members, 1963: Environmental and thunderstorm structures as shown by National Severe Storms Project observations in spring 1960 and 1961. *Mon. Wea. Rev.*, **91**, 271-292.

Ogura, Y., and Y. Chen, 1977: A life history of an intense mesoscale convective storm in Oklahoma. *J. Atmos. Sci.*, **34**, 1458-1476.

Papineau, J.M., 1992: A performance evaluation of the NGM and RAMS models for the 29-30 March 1991 Front Range storm. M.S. Thesis, Atmospheric Science Department, Colorado State University, 73 pp.

Parsons, D.B., M.A. Shapiro, R.M. Hardesty, and R.J. Zamora, 1991: The finescale structure of a west Texas dryline. *Mon. Wea. Rev.*, **119**, 1242-1258.

Pielke, R.A., 1974: A three-dimensional numerical model of the sea-breezes over south Florida. *Mon. Wea. Rev.*, **102**, 115-139.

Pielke, R.A., 1984: *Mesoscale Meteorological Modeling.* Academic Press, Orlando, Florida, 612 pp.

Pielke, R.A., and R. Avissar, 1990: Influence of landscape structure on local and regional climate. *Landscape Ecology*, **4**, 133-155.

Pielke, R.A., W.R. Cotton, R.L. Walko, C.J. Tremback, W.A. Lyons, L.D. Grasso, M.E. Nicholls, M.D. Moran, D.A. Wesley, T.J. Lee, and J.H. Copeland, 1992: A comprehensive meteorological system–RAMS. *Meteor. Atmos. Phys.*, **49**, 69-91.

Pielke, R.A., T.J. Lee, J.H. Copeland, J.L. Eastman, C.L. Ziegler, and C.A. Finley, 1994: Use of USGS-provided data to improve weather and climate simulations. *Ecological Appl.*, [in review].

Pielke, R.A., and M. Segal, 1986: Mesoscale circulations forced by differential terrain heating. In *Mesoscale Meteorology and Forecasting*, edited by P. S. Ray, Amer. Meteor. Soc., Boston, Mass., 516-548.

Pitman, A.J., 1994: Assessing the sensitivity of a land-surface scheme to the parameter values using a single column model. *J. Climate*, **7**, 1856-1869.

Pleim, J.E., and A. Xiu, 1995: Development and testing of a surface flux and planetary boundary layer model for application in mesoscale models. *J. Appl. Meteor.*, **34**, 16-32.

Rhea, J.O., 1966: A study of thunderstorm formation along drylines. *J. Appl. Meteor.*, **5**, 58-63.

Rust, W.D., R.P. Davies-Jones, D.W. Burgess, R.A. Maddox, L.C. Showell, T.C. Marshall, and D.K. Lauritsen, 1990: Testing a mobile version of a Cross-chain Loran Atmospheric Sounding System (M-CLASS). *Bull. Amer. Meteor. Soc.*, **71**, 173-180.

Schaefer, J.T., 1974: A simulative model of dryline motion. *J. Atmos. Sci.*, **31**, 956-964.

Schaefer, J.T., 1974: The life cycle of the dryline. *J. Appl. Meteor.*, **13**, 444-448.

Schaefer, J.T., 1975: Nonlinear biconstituent diffusion: A possible trigger of convection. *J. Atmos. Sci.*, **32**, 2278-2284.

Schaefer, J.T., 1986: The Dryline. In *Mesoscale Meteorology and Forecasting*, edited by P. S. Ray, Amer. Meteor. Soc., Boston, Mass., 549-570.

Segal, M., and R.W. Arritt, 1992: Nonclassical mesoscale circulations caused by surface sensible heat-flux gradients. *Bull. Amer. Meteor. Soc.*, **73**, 1593-1604.

Smith, C.B., M.N. Lakhtakia, W.J. Capehart, and T.N. Carlson, 1994: Initialization of soil-water content in regional-scale atmospheric prediction models. *Bull. Amer. Meteor. Soc.*, **75**, 585-593.

Stull, R.B., 1988: *An Introduction to Boundary Layer Meteorology.* Kluwer Academic Publishers, Norwell, Mass., 666 pp.

Sun, W.-Y., and Y. Ogura, 1979: Boundary layer forcing as a possible trigger to a squall-line formation. *J. Atmos. Sci.*, **36**, 235-254.

Sun, W.-Y., and C.-C. Wu, 1992: Formation and diurnal variation of the dryline. *J. Atmos. Sci.*, **49**, 1606-1618.

Tremback, C.J., and R. Kessler, 1985: A surface temperature and moisture parameterization for use in mesoscale models. *Proc. Seventh Conference on Numerical Weather Prediction*, Amer. Meteor. Soc., Boston, Mass., 355-358.

U.S. Department of Commerce and U.S. Department of Agriculture (USDOC/USDA), 1991: *Weekly Weather and Crop Bulletin*, **78**, 19.

Wakimoto, R.M., and N.T. Atkins, 1994: Observations of the sea-breeze front during CaPE. Part I: Single-Doppler, satellite, and cloud photogrammetry analysis. *Mon. Wea. Rev.*, **122**, 1092-1114.

Walko, R.L., C.J. Tremback, and R.F.A. Hertenstein, 1993: RAMS–The Regional Atmospheric Modeling System Version 3a: User's Guide. ASTeR, Inc., Fort Collins, CO., 100 pp.

Wetzel, P.J., and J.-T. Chang, 1988: Evapotranspiration from nonuniform surfaces: A first approach for short-term numerical weather prediction. *Mon. Wea. Rev.*, **116**, 600-621.

Yan, H., and R.A. Anthes, 1988: The effect of variations in surface moisture on mesoscale circulations. *Mon. Wea. Rev.*, **116**, 192-208.

Ziegler, C.L., and C.E. Hane, 1993: An observational study of the dryline. *Mon. Wea. Rev.*, **121**, 1134-1151.

Ziegler, C.L., T.J. Lee, and R.A. Pielke, 1994: Simulations of the dryline with a 3-D mesoscale model. *Preprints, 6th Conference on Mesoscale Processes*, Portland, OR., Amer. Meteor. Soc., P2.4.

Ziegler, C.L., W.J. Martin, R.A. Pielke, and R.L. Walko, 1994: A modeling study of the dryline. *J. Atmos. Sci.*, **52**, 263-285.

Zhang, D., and R.A. Anthes, 1982: A high resolution model of the planetary boundary layer–sensitivity tests and comparisons with SESAME-79 data. *J. Appl. Meteor.*, **21**, 1594-1609.

Appendix A

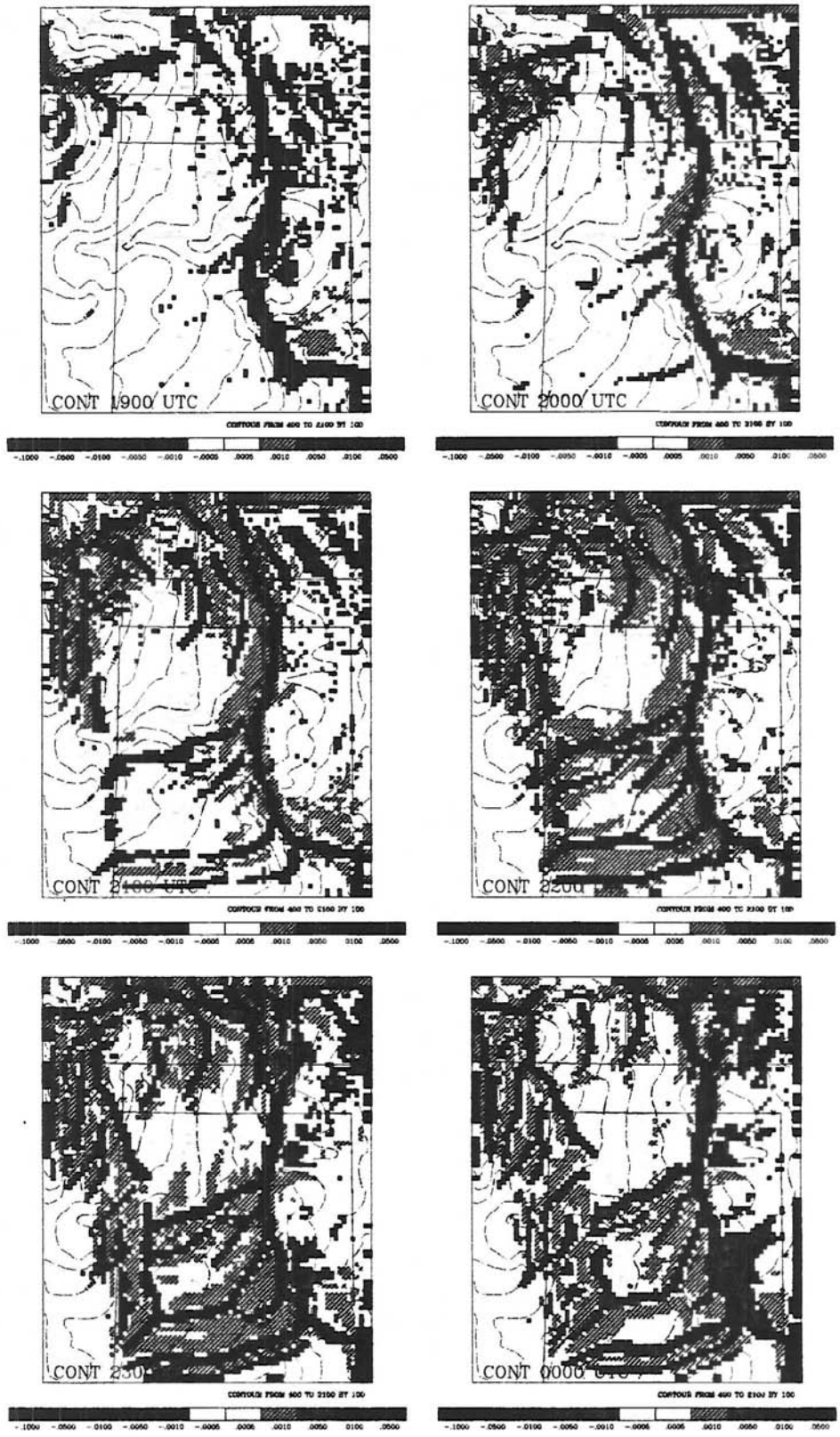

Figure A.1: Horizontal moisture flux divergence (g kg^{-1} s^{-1}) and topography (m) for the last 6 hours of the CONT simulation. Warm colors indicate moisture divergence.

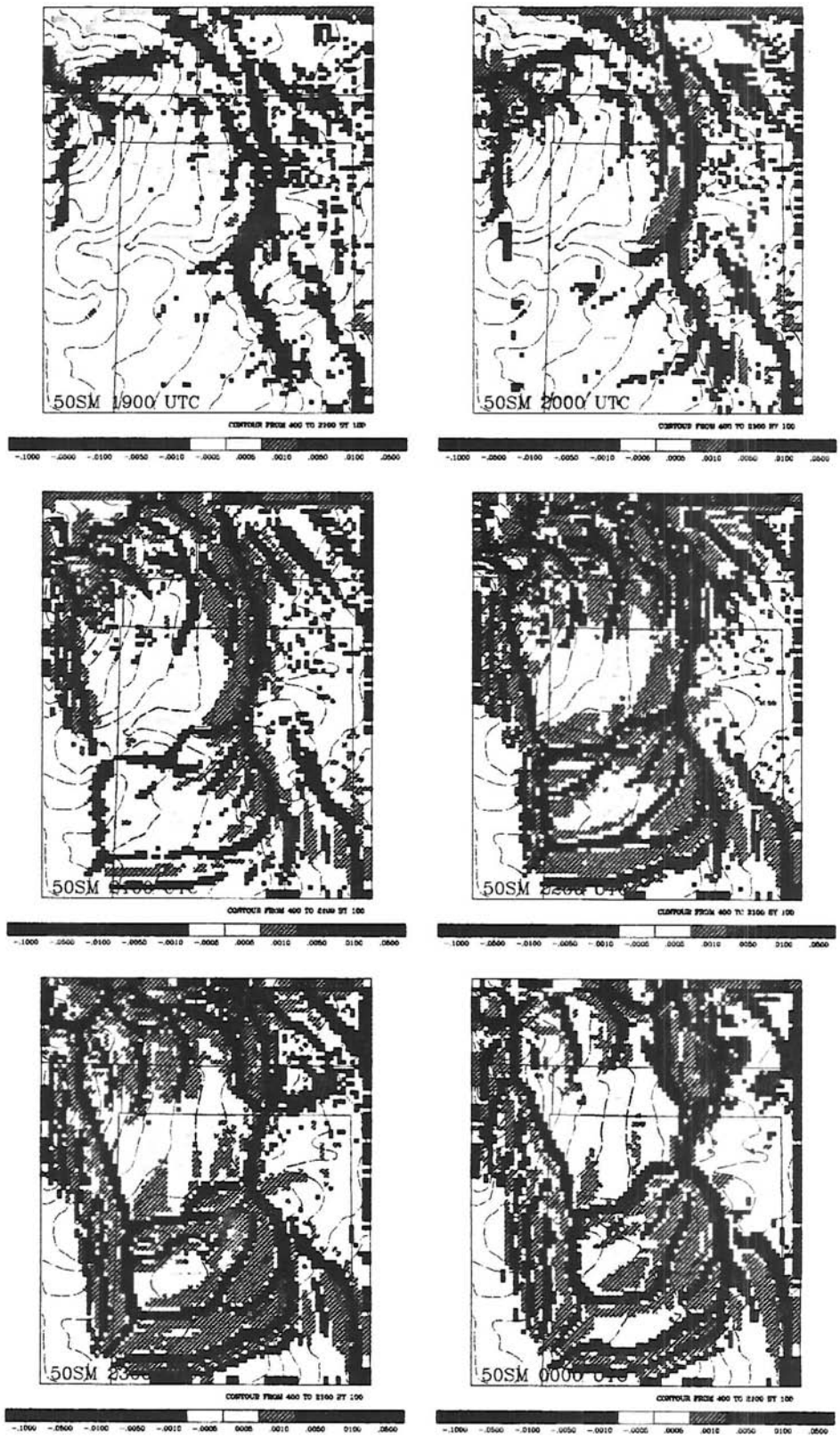

Figure A.2: Same as A.1, but for the 50SM simulation.

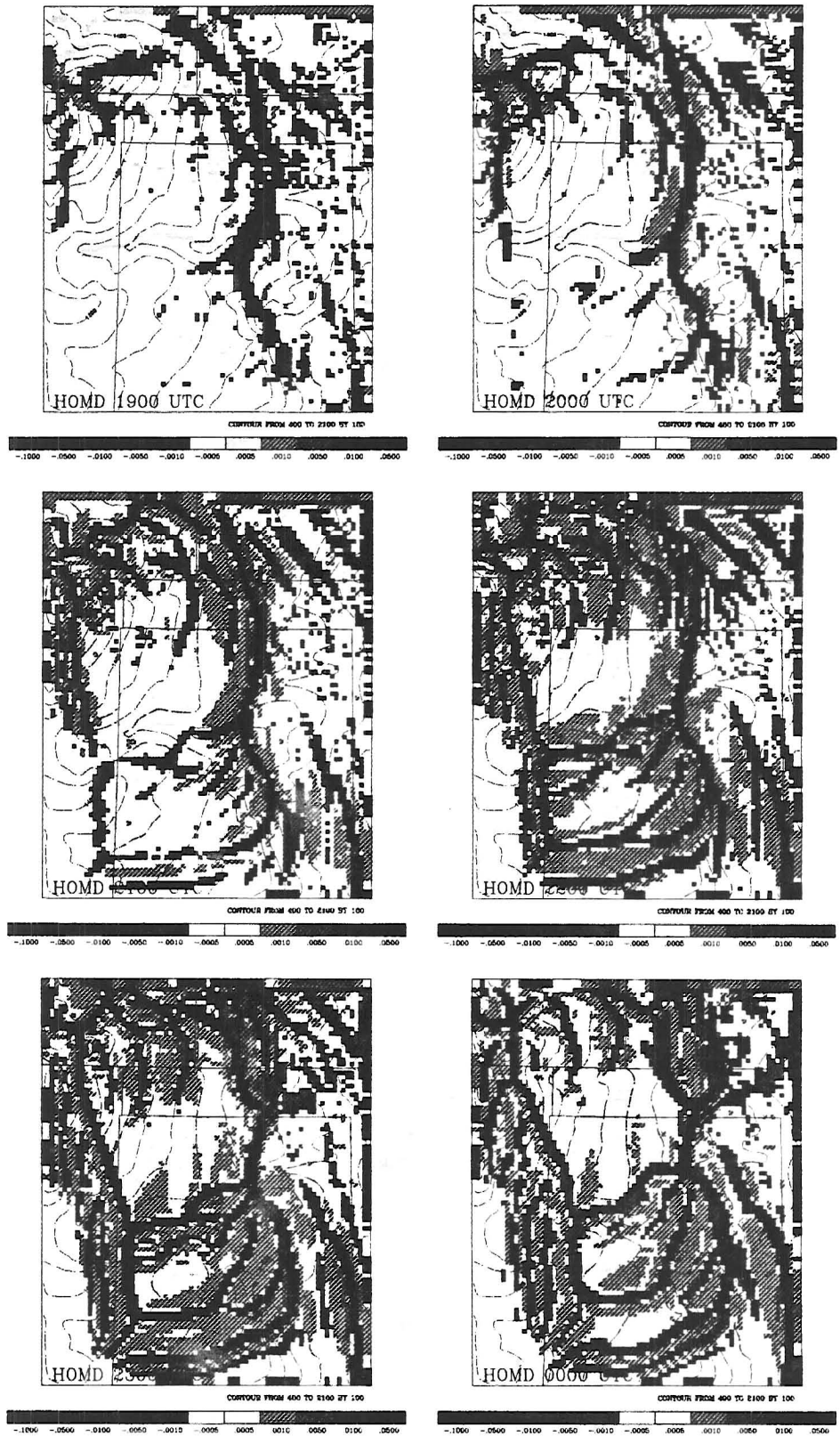

Figure A.3: Same as A.1, but for the HOMD simulation.